
CLOSING THE EVIDENCE GAP: REDDEMCEE, A FAST ADAPTIVE PARALLEL TEMPERING SAMPLER

Pablo A. Peña R. 

Instituto de Estudios Astrofísicos
Facultad de Ingeniería y Ciencias
Universidad Diego Portales
Av. Ejército 441, Santiago, Chile

James S. Jenkins 

Instituto de Estudios Astrofísicos
Facultad de Ingeniería y Ciencias
Universidad Diego Portales
Av. Ejército 441, Santiago, Chile

September 30, 2025

ABSTRACT

Markov Chain Monte Carlo (MCMC) excels at sampling complex posteriors but traditionally lags behind nested sampling in accurate evidence estimation, which is crucial for model comparison in astrophysical problems. We introduce `reddemcee`, an Adaptive Parallel Tempering Ensemble Sampler, aiming to close this gap by simultaneously presenting next-generation automated temperature-ladder adaptation techniques and robust, low-bias evidence estimators. `reddemcee` couples an affine-invariant stretch move with five interchangeable ladder-adaptation objectives—Uniform Swap Acceptance Rate, Swap Mean Distance, Gaussian-Area Overlap, Small Gaussian Gap, and Equalised Thermodynamic Length—implemented through a common differential update rule. Three evidence estimators are provided: Curvature-aware Thermodynamic Integration (TI+), Geometric-Bridge Stepping Stones (SS+), and a novel Hybrid algorithm that blends both approaches (H+). Performance and accuracy of the sampler are benchmarked on n-dimensional Gaussian Shells, Gaussian Egg-box, Rosenbrock Functions, and the real exoplanet radial-velocity time-series dataset of HD 20794. Across Shells up to 15 dimensions, `reddemcee` presents roughly 7 times the effective sampling speed of the best dynamic nested sampling configuration. The TI+, SS+ and H+ estimators recover estimates to within $|\Delta \ln \mathcal{Z}| \lesssim 3\%$ and supply realistic error bars with as few as six temperatures. In the HD 20794 case study, `reddemcee` reproduces literature model rankings and yields tighter yet consistent planetary parameters compared with `dynesty`, with evidence errors that track run-to-run dispersion. By unifying fast ladder adaptation with reliable evidence estimators, `reddemcee` delivers strong throughput and accurate evidence estimates, often matching, and occasionally surpassing, dynamic nested sampling, while preserving the rich posterior information which makes MCMC indispensable for modern Bayesian inference.

1 Introduction

In scientific research, any measured data needs to be tested with a suitable hypothesis. As such, robust statistical techniques are indispensable for parameter estimation and model comparison. Science frequently faces the challenge of characterising probability distributions arising from complex, high-dimensional models with nuisance parameters, uncertainties, and degeneracies. Markov Chain Monte Carlo (MCMC) methods are widely recognised as a vital tool in many areas of science. They enable researchers both to characterise parameter uncertainties precisely and to compare models rigorously. Research areas that rely on precise inference—such as phylogenetics [1, 2], physio-chemistry [3, 4], gravitational waves [5, 6], and exoplanet discovery [7, 8]—benefit from the flexibility of MCMC techniques to explore difficult posterior landscapes.

Early exoplanet radial-velocity (RV) detections were often confirmed by identifying significant peaks in periodograms—where false-alarm probabilities were calculated to establish the significance of the planetary candidate—and performing non-linear least-square fitting for Keplerian orbits. Such was the case for 51 Pegasi b [9]—the first exoplanet around a Sun-like star—and for the many Jovian planets that quickly followed this discovery [10, 11].

However, as RV data grew and multi-planet systems became common, more sophisticated statistical tools were needed to extract the more difficult exoplanet signals, which could be subtle, degenerate, and embedded in considerable noise. This led to the introduction of MCMC methods [12], revolutionising exoplanet RV fitting with robust estimation of orbital parameters with realistic uncertainties, even for non-linear parameters (like eccentricity and longitude of periastron). Far from perfect, MCMC still has its caveats. Poorly tuned chains could wander slowly or get trapped in local maxima.

To thoroughly explore multi-modal parameter spaces (common in multi-planet systems for example) [13] pioneered the use of the Parallel Tempering (PT) MCMC method [14, 15] in relation to RV signal detection and characterisation. This approach runs several chains in parallel to sample different powers (a temperature ladder) of the posterior distribution, each tempered to a different level. Hotter chains traverse the parameter space with more freedom, while colder chains sample the fine details. Inter-chain communication allows the sampler to explore distant high probability nodes with ease. Furthermore, PT enables the algorithm to estimate the marginalised posterior or evidence, a crucial quantity for model comparison. [13] shows that this method is capable of efficiently exploring all regions of the phase-space, lessening the burden of multi-modality. However, this early implementation was not capable of estimating the evidence reliably without a huge performance loss.

Affine-invariant ensemble samplers [16] also found their way into the exoplanet domain [17]. This MCMC variant, instead of a single chain, utilises simultaneously an ensemble of ‘walkers’, making the sampler insensitive to parameter covariances, while producing multiple samples per step, thus providing an enormous computational performance boost.

As an extra Keplerian in your model can always fit noise, efforts turned to provide an accurate model comparison framework, leading to the usage of nested sampling (NS) algorithms [18], to calculate the Bayesian evidence for competing models (with differing number of planets or noise models), allowing one to select the most likely one [19, 20]. Building on nested sampling, Dynamic Nested Sampling [DNS, 21, 22] introduces an adaptive allocation of ‘sampling effort’ to higher probability areas of the phase space, further increasing the efficiency of reaching the target evidence precision, finding use in RV fitting [23].

MCMC excels in parameter posterior estimation, yielding reliable uncertainties, even for complex or correlated parameters. However, while evidence estimation is certainly possible under this algorithm, it is as a by-product of the posterior exploration. Therefore, increasing the accuracy of the evidence estimation does not necessarily translate to an increased posterior accuracy, while carrying a substantial computational burden. On the other hand, NS is primarily designed for efficient evidence estimation by systematically shrinking the likelihood volume. As a by-product, it provides posterior samples, which can be used to model the parameter posteriors. Consequently, this method inherently does not provide as many samples from the parameter distribution as a well-tuned MCMC, conveying less precise parameter estimates.

This work presents `reddemcee`¹, an Adaptive Parallel Tempering MCMC python algorithm for any scientific sampling related endeavour that handles complex, high dimensional, multi-modal posteriors, with several competing models. Leveraging five different automated tuning strategies for the temperature ladder—two classic ones, uniform swap acceptance, and posterior area overlap, and three new implementations based on average energy differences, the system’s specific heat, and the swap mean distance—while providing original adaptations for evidence estimation, like the stepping stones algorithm [SS, 24] with a per-stone geometric-bridge, thermodynamic integration [TI, 25] enhanced by curvature-aware interpolation, as well as a novel hybrid approach.

2 Bayesian Framework

A full description of Bayesian inference or MCMC methods is beyond the scope of this manuscript, and we therefore refer the reader to [26]. Nonetheless, a summary of essential concepts is provided.

Bayesian inference generally consists of depicting the posterior probability distribution over the parameters $\boldsymbol{\theta} \in \Theta$ of the hypothesised model M depicting some known measured data D :

$$p(\boldsymbol{\theta} | D, M) = \frac{p(\boldsymbol{\theta} | M) \cdot p(D | \boldsymbol{\theta}, M)}{p(D | M)} \quad (1)$$

$p(\boldsymbol{\theta} | M)$ corresponds to the prior distribution; $p(D | \boldsymbol{\theta}, M)$ to the likelihood function, and $p(D | M)$ to the marginalised likelihood, frequently denoted as the Bayesian evidence \mathcal{Z} , or simply ‘evidence’ (as it will be in this work). Throughout this work, proper priors are assumed $\int_{\Theta} p(\boldsymbol{\theta} | M) = 1$ so the evidence is well-defined and finite.

¹<https://reddemcee.readthedocs.io/>

The evidence quantifies the overall support for model M and is crucial for Bayesian model comparison. However, the evidence integral generally has no closed-form solution and must be estimated numerically [27]. MCMC methods, while excelling at drawing samples from the posterior, do not directly provide \mathcal{Z} .

Within MCMC methods, several evidence estimation techniques have been developed [28]. For parallel tempering MCMC, two common approaches are the thermodynamic integration [25] and stepping stones [24]. How parallel tempering works and how TI and SS leverage the tempered ensemble to estimate the evidence is briefly outlined below.

2.1 Parallel Tempering MCMC

PT MCMC runs an ensemble of B parallel chains, each sampling a different power of the posterior distribution (at a different temperature T_i ; 14, 15, 29). The inverse of the temperature is $\beta = \frac{1}{T}$, with $1 = \beta_1 > \beta_2 > \dots > \beta_{B-1} > \beta_B \geq 0$, and the full chain $\bar{X}_t = (X_t^{(\beta_1)}, \dots, X_t^{(\beta_B)})$. By convention, $\beta_1 = 1$ for the cold chain (sampling the original posterior), and $\beta_B \approx 0$ for the hottest chain (sampling a highly flattened landscape, approaching the prior as $\beta_B \rightarrow 0$). Each chain $X_t^{(\beta_i)}$ samples a tempered posterior where the likelihood has been raised to the power β_i :

$$\mathcal{P}_{\beta_i}(\boldsymbol{\theta}) = \frac{\Pi \cdot \mathcal{L}^{\beta_i}}{\mathcal{Z}_{\beta_i}} \quad (2)$$

Where $\mathcal{P}_{\beta_i}(\boldsymbol{\theta})$ is the posterior distribution, Π the prior, \mathcal{L}^{β_i} the tempered likelihood, and \mathcal{Z}_{β_i} the evidence.

In $\mathcal{P}_{\beta}(\boldsymbol{\theta})$, hotter temperatures have the effect of flattening and broadening peaks, reducing local maxima trapping and effectively making the posterior easier to sample. As such, hot chains are able to rapidly sample a large portion of the parameter space, whilst cold chains, provide precise local sampling. By allowing chains at different temperatures to swap states, PT achieves a fast, thorough sampling of the posterior. Swaps in PT are implemented with a Metropolis-like acceptance rule. The pairwise swap [30], which is when two adjacent chains $(X_t^{(\beta_i)}, X_t^{(\beta_{i+1})})$ propose to switch states with probability:

$$A_{i,i+1} = \min \left(0, -\Delta \ln \mathcal{L}^{\beta_i} \cdot \Delta \beta_i \right) \quad (3)$$

With $\Delta \ln \mathcal{L}_i$ the log-likelihood difference between the two chain states. This criterion (derived by simplifying the detailed balance condition for swapping two Boltzmann-distributed ensembles) shows that swaps are more probable when a high-likelihood state from a hotter chain is proposed for a colder chain. Without adjacent posteriors overlapping enough to allow regular swaps, efficiency plummets. By tuning the temperature ladder (the set of β_i values), PT aims to maintain a reasonably high swap acceptance rate across all adjacent pairs, ensuring a thorough exploration of the posterior landscape, and providing a natural framework for estimating the evidence \mathcal{Z} via the ladder of tempered distributions.

Although our APT implementation does not provide independent draws, we will set up the classic methods for evidence estimation next, which do assume iid-based errors, and in §3.3 we address how to handle this problem.

2.2 Thermodynamic Integration

Thermodynamic integration [25, 30, 31] is a an indirect method to compute the evidence \mathcal{Z} by leveraging the continuous sequence of intermediate posteriors between prior and posterior. The basic formula arises from the identity (in statistical mechanics) that relates the derivative of the log-partition function to the average energy. In Bayesian terms:

$$\ln \mathcal{Z} = \ln \mathcal{Z}_1 - \ln \mathcal{Z}_0 = \int_0^1 \mathbb{E}_{\beta} [\ln \mathcal{L}] d\beta \quad (4)$$

where $\mathbb{E}_{\beta} [\dots]$ is the expectation with respect to $\mathcal{P}_{\beta_i}(\boldsymbol{\theta})$, the tempered posterior at inverse temperature β . Since $\mathcal{Z}_0 = 1$ for proper priors, so $\ln \mathcal{Z}_0 = 0$, and the integral directly yields $\ln \mathcal{Z}$. With B the number of temperatures, the integral is calculated via the trapezoidal rule:

$$\ln \hat{\mathcal{Z}}_{\text{TI}} \approx \sum_{i=1}^{B-1} \frac{\mathbb{E}_{\beta_{i+1}} [\ln \mathcal{L}] + \mathbb{E}_{\beta_i} [\ln \mathcal{L}]}{2} \cdot \Delta \beta_i \quad (5)$$

2.3 Stepping Stones

The stepping-stones algorithm [24] estimates the evidence ratio $\mathcal{Z} = \mathcal{Z}_1 / \mathcal{Z}_0$ into a telescopic product across the temperature ladder:

$$\hat{\mathcal{Z}}_{\text{SS}} = \prod_{i=1}^{B-1} \frac{\mathcal{Z}_{\beta_i}}{\mathcal{Z}_{\beta_{i+1}}} = \prod_{i=1}^{B-1} r_i; \quad r_i \equiv \frac{\mathcal{Z}_{\beta_i}}{\mathcal{Z}_{\beta_{i+1}}} = \mathbb{E}_{\beta_{i+1}} [\mathcal{L}^{\beta_i - \beta_{i+1}}] \quad (6)$$

with r_i the stepping-stones ratios and $\mathbb{E}_{\beta} [\dots]$ the expectation with respect to $\mathcal{P}_{\beta_i}(\boldsymbol{\theta})$. It is often convenient to work in log-space for numerical stability, yielding

$$\ln \hat{\mathcal{Z}}_{\text{SS}} = \sum_{i=1}^{B-1} \ln \left[\frac{1}{N_i} \sum_{n=1}^{N_i} \mathcal{L}^{\beta_i - \beta_{i+1}} \right] \quad (7)$$

where N_i is the number of posterior samples per chain used to approximate each expectation. SS has the advantage of typically yielding improved accuracy over TI when the number of temperatures is limited, since it more directly ‘bridges’ distributions to evaluate each incremental evidence ratio.

2.4 Evidence Error Estimation

For TI, [31] identify two sources of error: one from the sampling itself $\hat{\sigma}_S$, calculated as the MC standard error affecting the log-likelihood averages, and another from the discretisation of the integral $\hat{\sigma}_D$. This quantity can be estimated by considering the worst-case contribution of the trapezoidal rule (essentially misrepresenting the whole triangular part):

$$\hat{\sigma}_D \simeq \frac{|\mathbb{E}_{\beta_i} [\ln \mathcal{L}] - \mathbb{E}_{\beta_{i+1}} [\ln \mathcal{L}]|}{2} \cdot \Delta\beta_i \quad (8)$$

For the SS method, the product of unbiased estimators $\hat{\mathcal{Z}}_{\text{SS}}$ is also unbiased, nevertheless, changing to log-scale introduces one. [24] estimates the error as:

$$\hat{\sigma}_{\mathcal{Z}_{\text{SS}}}^2 \approx \frac{1}{N^2} \sum_{i=1}^{B-1} \sum_{n=1}^N \left(\frac{\mathcal{L}^{\beta_i - \beta_{i+1}}}{\hat{r}_i} - 1 \right)^2 \quad (9)$$

3 Temperature Ladder

By extending the parallelisms with statistical thermodynamics, where the specific heat C_v is defined by the energy $U = -\ln \mathcal{L}$:

$$C_v(\beta) = \frac{d\mathbb{E}_{\beta}[U]}{dT} = \beta^2 (\mathbb{E}_{\beta}[U^2] - \mathbb{E}_{\beta}[U]^2) = \beta^2 \text{Var}_{\beta}[U] \quad (10)$$

This quantity governs the energy fluctuations at different temperatures, and is closely related to both the temperature ladder and the swap acceptance rate. The mean Swap Acceptance Rate (SAR)—derived from Eq.3—for a small temperature gap can be expressed as:

$$\begin{aligned} \bar{A}_{i,i+1} &= \mathbb{E}_{\beta_i, \beta_{i+1}} [\exp(-\Delta U_i \cdot \Delta\beta_i)] \\ &\propto \mathbb{E}_{\beta_i} [\Delta U_i \cdot \Delta\beta_i] = \frac{\sqrt{C_v(\beta_i)}}{\beta_i} \Delta\beta_i \end{aligned} \quad (11)$$

In the PT scheme, the temperature ladder must be chosen to maximise the efficiency of the cold chain. To ensure this chain has good mixing, from the SAR (see Eq.11), it would suffice to minimise both $\Delta\beta_i$ and ΔU_i for every single chain, this way, samples from the hot chain can easily traverse to the cold chain. As a secondary aim, the temperature ladder serves to estimate the evidence as well, so allocating the temperatures aiming to convenience either the TI or the SS methodologies also has its benefits. Achieving a Uniform SAR across all chains is generally considered a good strategy for healthy mixing [4, 32, 33, 34, 35].

3.1 Geometric Spacing

[36] and later [32], by analysing the constant specific heat scenario, conclude that adjacent temperatures geometrically spaced should approximate to a uniform SAR. With a constant ratio \bar{R} , each β would be defined by:

$$\bar{R} = \frac{\beta_i}{\beta_{i+1}} \quad (12)$$

This is the starting point for ladder design. And the reason why adaptive methods are needed: geometric spacing assumes constant C_ν , which does not hold true in complex posteriors.

3.2 Adaptive Methods

The Adaptive Parallel Tempering (APT) MCMC [37, 34, 29, 35] dynamically updates the temperatures alongside the run, aiming to improve the mixing efficiency. Such an algorithm inherently fails to be ergodic and possibly to preserve the stationarity of the cold chain. In practice, `reddemcee` uses a decaying adaptive rate (see Eq.14), allowing the ladder to stabilise over time. Then, the adaptation can be discontinued, from where detailed balance is preserved and standard ergodicity theorems apply. Next, five different adaptation strategies are shown, of which the first two—Uniform Swap Acceptance Rate, and Gaussian Area Overlap—are commonly seen in the literature, while for the latter three—Swap Mean Distance, Small Gaussian Gap, and Equalised Thermodynamic Length—we present our implementations, as alternatives, especially when C_ν is non-uniform.

3.2.1 Uniform Swap Acceptance Rate

[35] propose that the temperature ladder dynamic adjustments are guided by the SAR. They define the ladder in terms of logarithmic temperature intervals S_i between adjacent chains. Therefore, the adaptation rate corresponds to $\frac{dS_i}{dt}$. The adaptation includes a diminishing factor $\kappa(t)$, where $\lim_{t \rightarrow \infty} \kappa(t) = 0$, here expressed as a hyperbolic decay:

$$S_i \equiv \ln(T_i - T_{i+1}); \quad \frac{dS_i}{dt} = \kappa(t) [A_i(t) - A_{i+1}(t)] \quad (13)$$

$$\kappa(t) = \frac{1}{\nu_0} \frac{\tau_0}{(t + \tau_0)} \quad (14)$$

With $A_i(t)$ the measured SAR, τ_0 the decay half-life, and ν_0 the evolution time-scale. This leaves both β_1 and β_B static, while the intermediate temperatures settle to achieve an uniform SAR.

3.2.2 Gaussian Area Overlap

[38], by studying the correlation between replicas of the SAR and the area of overlap of likelihoods in Gaussian distributions, found a relation to control acceptance rate by temperature spacing:

$$A_{\text{overlap}} = \text{erfc} \left[\frac{\Delta \ln \mathcal{L}}{2\sqrt{2}\sigma_m} \right] \quad \Rightarrow \frac{\Delta \ln \mathcal{L}}{\sigma_m} \Big|_{\beta_i} = \left[\frac{\Delta \ln \mathcal{L}}{\sigma_m} \right]_{\text{target}} \quad (15)$$

Where $\sigma_m = (\sigma_1 + \sigma_2)/2$, the mean of the deviations of the adjacent temperature log-likelihoods. While also aiming for Uniform SAR, the ladder evolution is informed by a different mechanism, which may compensate the effects of having a non-uniform C_ν .

3.2.3 Uniform Swap Mean Distance

Considering that a non-uniform C_ν is more realistic for complex systems (as in exoplanet discovery), [39] present the feedback optimised method, which maximises the round trips of each replica between the extremal temperatures. This would lead to information of the likelihood landscape going faster from the hot to the cold chain. A well tempered chain (where the posterior shape has changed significantly compared to the target posterior) should propose far away states which, if accepted, would contribute more to healthy mixing than a swap so close that it is equivalent to the intra-chain evolution. Therefore, a ladder where adjacent swaps are done by maximising the swap distance would maximise the crossing of ‘useful’ information across the replicas. By normalising to unity all dimensions in the system, the mean distance of adjacent swaps for all walkers for a given temperature is taken into account:

$$d|_{\beta_i} = \frac{1}{W} \sum_{w=1}^W \sqrt{\sum_{d=1}^D \left(\frac{\theta_{d,i} - \theta_{d,i+1}}{c_d} \right)^2} \quad (16)$$

Where W is the number of walkers, D the number of dimensions, and c_d the range of the prior for dimension d . Hereafter this method is referred to as the Swap Mean Distance (SMD). Intuitively, this encourages swaps that carry proposals farther across the parameter space, which may be specifically beneficial in high-dimensional problems, where local swaps might exchange nearly similar states.

3.2.4 Small Gaussian Gap

This scheme (SGG) targets a uniform SAR by using a Gaussian approximation for small temperature gaps. If adjacent β s are very close, the energy difference ΔU_i has approximately a Gaussian distribution $\sim \mathcal{N}(0, 2\text{Var}[U_i])$. In this small-gap regime, one can show that the product $(\Delta\beta_i)^2 \text{Var}[U_i]$ largely controls the swap acceptance rate [32], from Eq.11:

$$\begin{aligned} \bar{A}_{i,i+1} &= \mathbb{E}_{\beta_i, \beta_{i+1}} [\exp(-\Delta U_i \cdot \Delta\beta_i)] \\ &\approx \exp\left(\frac{1}{2}(\Delta\beta_i)^2(2\text{Var}_{\beta_i}[U])\right) = \exp((\Delta\beta_i)^2(\text{Var}_{\beta_i}[U])) \end{aligned} \quad (17)$$

Thus, keeping the product $(\Delta\beta_i)^2(\text{Var}[U_i])$ constant imply a roughly uniform SAR.

3.2.5 Equalised Thermodynamic Length

The thermodynamic length is defined as:

$$L(\beta) = \int_{\beta_{\min}}^{\beta_{\max}} \sqrt{\text{Var}_{\beta}[U]} d\beta = \int_{\beta_{\min}}^{\beta_{\max}} \frac{\sqrt{C_v}(\beta)}{\beta} d\beta \quad (18)$$

Intuitively $L(\beta)$ corresponds to the local metric which measures how quickly (or far) the distribution changes with β . Setting neighbouring replica' distributions so they are the same 'distance' apart translates to placing them uniformly in L -space, effectively populating the regions where C_v peaks with more chains. This ensures denser sampling where the posterior changes most rapidly. Each interval of this integral can be approximated as:

$$\Delta L_i \approx \frac{\Delta\beta_i}{2} (\sqrt{\text{Var}_{\beta_i}[U]} + \sqrt{\text{Var}_{\beta_{i+1}}[U]}) \quad (19)$$

Then the discrete estimate for thermodynamic distance:

$$L(\beta_N) = \sum_{i=0}^{B-1} \Delta L_i \quad (20)$$

[40] arrives at the same conclusion, further demonstrating that under constant C_v , the ETL forms a geometric progression as well.

3.2.6 Ladder Adaptation in `reddemcee`

`reddemcee` implements each of the methods discussed above by setting the adaptation as $\frac{dS_i}{dt} = \kappa(t) \cdot Q_i$. This way, defining Q_i will set the desired adaptive approach for the Uniform Swap Acceptance Rate (SAR), the Gaussian Area Overlap (GAO), the Uniform Swap Mean Distance (SMD), the Small Gaussian Gap approximation (SGG), or Equalised Thermodynamic Length (ETL):

$$Q_i = \begin{cases} [A_i(t) - A_{i+1}(t)] & \text{for SAR (see §3.2.1)} \\ \frac{\Delta U_i}{\sigma_m} & \text{for GAO (see §3.2.2)} \\ d|_{\beta_i} & \text{for SMD (see §3.2.3)} \\ \exp((\Delta\beta_i)^2(\text{Var}[U_i])) & \text{for SGG (see §3.2.4)} \\ \frac{\Delta L_i}{L(\beta_N)} & \text{for ETL (see §3.2.5)} \end{cases} \quad (21)$$

3.3 Revisiting Evidence

The APT implementation does not provide independent draws; each walker's proposal is based on its current position, meaning successive samples retain memory until past the integrated autocorrelation time, the stretch move also couples walkers, influencing each others proposals [16]. Furthermore, the swap move creates a cross-temperature coupling as well. To account for all these effects in correlated draws, we replace iid-based errors with autocorrelation-adjusted MC standard errors [41] by using overlapping batch means [OBM, 42], which are consistent for MCMC under standard ergodicity conditions, and propagate cross-temperature covariance across the ladder. We use this as $\hat{\sigma}_S$ for both methods.

Both SS and TI rely on the shape of the $\mathbb{E}_\beta[U](\beta)$ curve, for which three factors can be considered: 1) The ladder size is relatively small, providing few samples for either TI or SS. 2) Temperatures are not uniformly spaced. 3) $\mathbb{E}_\beta[U](\beta)$ is a monotonic increasing function.

With these points in mind, two different solutions for a better $\hat{\sigma}_D$ come to mind. Using the Richardson extrapolation, which means computing the evidence estimate with two different grids, a coarse grid and a fine one. The difference is then used to extrapolate the discretisation error, leveraging the known order of convergence of the trapezoidal rule. On the other hand, estimating the local curvature of the curve—since the leading error term in the trapezoidal rule is proportional to the second derivative—for a tailored error estimate for each interval. In the following paragraphs two different original implementations are presented which leverage the known information about $\mathbb{E}_\beta[U](\beta)$ for a more precise $\ln \mathcal{Z}$ estimation.

Piecewise Interpolated Thermodynamic Integration Building on the TI method, an interpolation on the curve $\mathbb{E}_\beta[U](\beta)$ is applied with the local Piecewise Cubic Hermite Interpolating Polynomial (PCHIP), which preserves monotonicity (physically expected) and prevents overshooting for non-smooth data (few temperatures; 43).

For $\hat{\sigma}_D$, we form a coarse ladder by dropping every other temperature, build the corresponding PCHIP, and compute another coarser evidence estimate. We use its difference with respect to the finer one as the discretisation error.

The total error therefore corresponds to $\hat{\sigma}_{\mathcal{Z}} = \sqrt{\hat{\sigma}_D^2 + \hat{\sigma}_S^2}$. It is worth noting that this approach addresses the discretisation error more explicitly, thus reducing bias at the cost of possibly smaller (but more realistic) error bars, as shown in Section 4. More details on the method can be found in 11.2.

Geometric-Bridge Stepping Stones The SS evidence estimator $\hat{\mathcal{Z}}_{\text{SS}}$ (see Eq.9) estimates the ratio r_i with an expectation under a single distribution $\mathbb{E}_{\beta_{i+1}}[\cdot]$ (see Eq.6). We replace the ratios with geometric-bridge sampling [44, 45]:

$$r_i = \frac{\mathbb{E}_{\beta_i} [\mathcal{L}^{\Delta\beta_i/2}]}{\mathbb{E}_{\beta_{i+1}} [\mathcal{L}^{-\Delta\beta_i/2}]} \quad (22)$$

By using samples from both ends, we expect to diminish the estimator variance when the temperature gap is large, as the per-stone ratio would degrade less rapidly. Using the same APT samples has no additional computational cost, and by halving the exponent we reduce the dynamic range, improving numerical stability. More details in Appendix 11.1.

3.3.1 Hybrid Method

Consider a temperature mid-point, so thermodynamic integration is applied from $\beta \in [0, \beta_*]$, and stepping stones from $\beta \in [\beta_*, 1]$. Provided that continuity is ensured around β_* , separating where each method is stronger leads to a fair estimation of $\ln \mathcal{Z}$. From Eq.5 the overall log-evidence can be decomposed as:

$$\ln \mathcal{Z} = \int_0^1 \mathbb{E}_\beta [U] d\beta = \int_0^{\beta_*} \mathbb{E}_\beta [U] d\beta + \int_{\beta_*}^1 \mathbb{E}_\beta [U] d\beta \quad (23)$$

The transition between the ‘pure prior’ region ($\beta=0$) to a moderately informed distribution (small β) generally changes statistics more dramatically than other areas. Intuitively, any sharp change in posterior shape can be seen as a phase transition, which is also reflected as a peak in $C_v(\beta)$. Since most temperature ladders are proportional in some form to C_v , chains are denser in this region, and therefore, a straightforward method like TI works well. Near $\beta=1$, SS is more efficient at handling ratios since the posterior is strongly peaked and $\Delta\beta$ tends to increase. By decomposing the TI trapezoidal area contribution of each interval, the mid-point is selected to be where the rectangular area is larger than twice the triangular area, ensuring we are in a region where ΔU_i dominates over $\Delta\beta_i$, and where the energy slope is pronounced:

$$\Delta\beta_i \cdot U_i \geq 2(\Delta\beta_i \cdot \frac{\Delta U_i}{2}) \Rightarrow 2U_i \geq U_{i+1} \quad (24)$$

4 Benchmarks

This section seeks to validate the proposed ladder adaptation algorithms as well as the evidence estimators. Taken together, these tests probe the different problems that matter most when contrasting an APT sampler with DNS. Gaussian Shells, Gaussian Egg-box, and the Hybrid Rosenbrock function will capture the three classic challenges when sampling from a multimodal distribution: mode-finding, mode-hopping, and in-mode mixing, all of which are intensified as dimensionality increases. Hereafter two distinct qualities will be compared. First, the sampler performance, comprised of both the intra-chain mixing and the computational cost, measured by the effective sample size (in thousands per second, dubbed ‘kenits’). And second, the evidence estimation, comprised of the evidence estimate and its error. This will be measured by both the difference found with the analytical evidence $\Delta_Z \equiv \exp(\ln Z - \ln \hat{Z}) - 1$, validating the accuracy of the estimator, and the log-likelihood $\mathcal{L}(\hat{Z}) \equiv \ln \mathcal{L}_{\hat{Z}}$, validating the credibility of the uncertainties, for $\ln \hat{Z} \sim \mathcal{N}(\ln \hat{Z}, \hat{\sigma}_{\ln \hat{Z}})$, where $\ln \hat{Z}$ is the estimate of the evidence, and $\hat{\sigma}_{\ln \hat{Z}}$ the estimate of the evidence uncertainty.

Each benchmark is run 11 times with different known random seeds, and the reported values correspond to the mean and standard deviation of all runs.

4.1 n-d Gaussian Shells

An analytically tractable problem that has been widely used in the literature is to sample from a n-dimensional Gaussian shell [19, 22]. The likelihood contours are curved, thin, and nearly singular (see Fig.1). Random-walk steps are inefficient, so this multimodal function stresses proposal geometry and temperature allocation. The likelihood is given by:

$$p(\vec{\theta}) = \sum_{i=1}^n \frac{1}{\sqrt{2\pi w^2}} \exp\left(-\frac{(|\vec{\theta} - \vec{c}_i| - r)^2}{2w^2}\right) \quad (25)$$

With n dimensions, r corresponding to the radius, w the width, and \vec{c}_i to the constant vectors describing the centres of the peaks.

This benchmark is used to assess the behaviour of the different samplers in both efficiency and evidence estimation. `reddemcee` was set up to work with an arbitrary number of iterations of [16, 320, 640, 1] temperatures, walkers, sweeps, and steps, respectively, for a grand-total of 3,276,800 samples. The adaptation hyper-parameters τ_0, ν_0 are set as one-tenth of the sweeps and one-hundredth of the walkers, respectively. For the temperatures to settle, we let the adaptation for half the sweeps, and freeze the ladder. We consider this initial phase as burn-in, and these samples are dropped out before any statistical inferences are made, but are still considered for the total quoted run-time (ie, the kenits run-time). On the other hand, the DNS algorithm was performed with `dynesty` [22], running three different sampling methods—uniform, slice, and random-slice, with its automated setup.

For calculating the kenits, `dynesty`’s reported number of calls was utilised, corresponding to the efficiency times all likelihood evaluations over total run-time, while for `reddemcee`, efficiency was taken as the inverse of the average autocorrelation time across parameters for the cold-chain, while kenits were calculated as the efficiency times used likelihood evaluations (discarding the burn-in samples, but not their run-time) over the full run-time. This method ensures a fair kenits comparison.

Sampler performance (see Table 1), all adaptive ladder methods are statistically similar; variance between ladder algorithms (0.04^2) is smaller than the run-to-run variance of each method ($\approx 0.12^2$), delivering ≈ 3.6 -3.8 kenits. The best DNS method, `dyn-rs`, scores 0.94 ± 0.05 kenits, $\sim 26\%$ of the APT average. This method also finishes the fastest, at ~ 13.4 s. It is worth mentioning that once converged, the efficiency does not radically change, so even by demanding a higher total iteration count as a stop condition, the kenits (and efficiency) would not dramatically increase. The dynamic algorithm stops at target precision, which in `dyn-u` case required much longer run-time with more samples, whereas the sampling efficient slice methods finished faster with far fewer independent samples. In other words, there is a trade off between posterior sampling at the expense of evidence estimation speed. The same reasoning can be extended to MCMC, preserving much richer posterior information.

Evidence estimation, the proposed evidence estimation methods in §2.4 are tested and compared against the analytical value for the 2-d case, $\ln Z = -1.746$ (see Table 2). The default TI method has $\Delta_Z|_{TI} = 8.394\%$, while the interpolated version has $\Delta_Z|_{TI+} = 0.324\%$, an order of magnitude closer to the true value. The likelihood improves as well, with a ratio of $\exp(2.80 - 0.92) = 6.58$. On the other hand, the default SS has the highest $\mathcal{L}(\hat{Z})|_{SS} = 4.326$ and a low

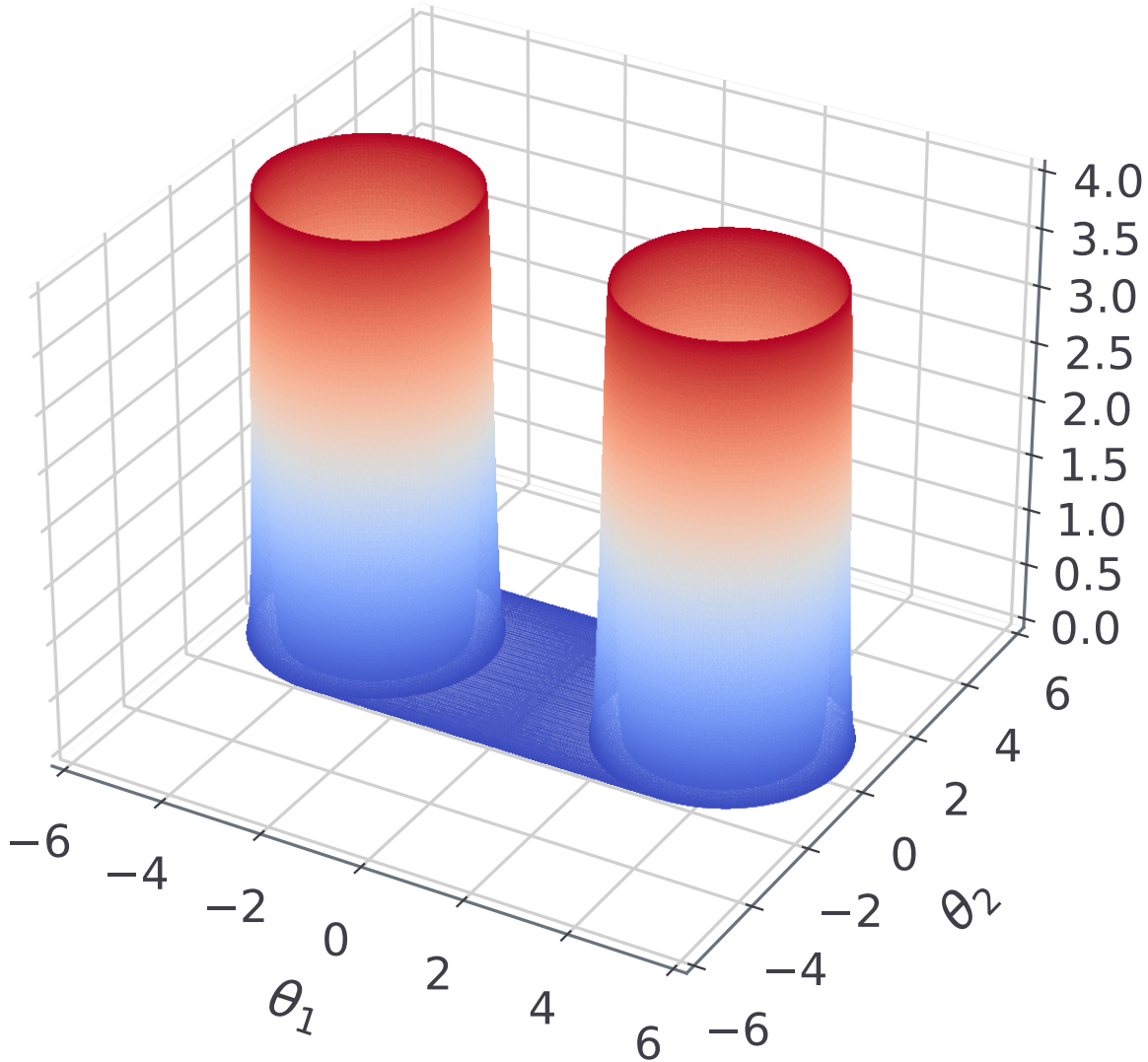


Figure 1: 2-d Gaussian shells likelihood. With radius $r=2$ and width $w=0.1$. Parameter space boundaries are imposed as ± 6 . Likelihood values are coloured from blue (low) to red (high) to facilitate the visualisation of the figure's shape.

Table 1: 2-d Gaussian Shells performance benchmark. `reddemcee`'s adaptive algorithms compared to `dynesty`'s uniform (dyn-u), slice(dyn-s), and random-slice (dyn-rs) sampling methods. From left to right: Time–total run time in seconds, Eff–sampling efficiency or percentage of independent samples, and Kenits–effective samples per second in thousands.

Method	Time (s)	Eff (%)	Kenits
SAR	37.60 \pm 0.28	8.49 \pm 0.27	3.70 \pm 0.12
SMD	37.77 \pm 0.19	8.59 \pm 0.27	3.73 \pm 0.13
SGG	37.86 \pm 0.15	8.49 \pm 0.30	3.67 \pm 0.13
GAO	37.95 \pm 0.25	8.34 \pm 0.25	3.60 \pm 0.11
ETL	37.94 \pm 0.22	8.49 \pm 0.24	3.66 \pm 0.10
dyn-u	68.66 \pm 16.75	4.94 \pm 0.82	0.19 \pm 0.04
dyn-s	16.83 \pm 0.89	3.77 \pm 0.22	0.75 \pm 0.04
dyn-rs	13.41 \pm 0.64	4.49 \pm 0.33	0.94 \pm 0.05

Table 2: 2-d Gaussian Shells SAR evidence estimation comparison. `reddemcee`'s adaptive algorithms compared to `dynesty`'s uniform (dyn-u), slice(dyn-s), and random-slice (dyn-rs) sampling methods. From left to right, the log-evidence estimator, the estimator uncertainty, the difference to the true value $\ln \mathcal{Z} = -1.746$ in percentage $\Delta_{\mathcal{Z}}$, and the log-likelihood of the estimator $\mathcal{L}(\hat{\mathcal{Z}})$.

Method	$\ln \hat{\mathcal{Z}}$	$\hat{\sigma}_{\ln \hat{\mathcal{Z}}}$	$\Delta_{\mathcal{Z}}(\%)$	$\mathcal{L}(\hat{\mathcal{Z}})$
TI	-1.833 \pm 0.008	0.066 \pm 0.005	8.394	0.917
SS	-1.744 \pm 0.008	0.005 \pm 0.001	0.117	4.326
H	-1.788 \pm 0.008	0.134 \pm 0.005	4.124	1.044
TI+	-1.749 \pm 0.008	0.024 \pm 0.005	0.324	2.801
SS+	-1.745 \pm 0.008	0.006 \pm 0.001	0.099	4.263
H+	-1.745 \pm 0.008	0.008 \pm 0.002	0.016	3.951
dyn-u	-1.763 \pm 0.054	0.040 \pm 0.001	1.751	2.206
dyn-s	-1.774 \pm 0.055	0.040 \pm 0.001	2.876	2.049
dyn-rs	-1.767 \pm 0.043	0.040 \pm 0.001	2.159	2.157

$\Delta_{\mathcal{Z}}|_{\text{SS}}=0.117\%$. The SS+ counterpart presents slightly more conservative uncertainties (0.006 instead of 0.005) with $\mathcal{L}(\hat{\mathcal{Z}})|_{\text{SS+}}=4.263$, and slightly better accuracy $\Delta_{\mathcal{Z}}|_{\text{SS+}}=0.099\%$. The H+ method has the highest accuracy of all $\Delta_{\mathcal{Z}}|_{\text{H+}}=0.016\%$, with a very high likelihood as well $\mathcal{L}(\hat{\mathcal{Z}})|_{\text{H+}}=3.951$. Out of the DNS methods, dyn-u is the most reliable with $\Delta_{\mathcal{Z}}|_{\text{dyn-u}}=1.751\%$, and a log-likelihood of $\mathcal{L}(\hat{\mathcal{Z}})|_{\text{dyn-u}}=2.206$.

4.2 Gaussian Egg-box

The Gaussian Egg-box, dubbed after its likelihood shape (see Fig 2), presents a periodic landscape with several equally heightened peaks, separated by deep troughs. It is an ideal stress-test for mode-completeness. Missing a single peak would render a catastrophically wrong evidence. The likelihood function is given by:

$$p(\vec{\theta}) = (2 + \prod_{n=1}^{\dim} \cos(\frac{\theta}{4}))^{\bar{\beta}_e} \quad (26)$$

Where $\bar{\beta}_e = 5$ is used, defining the narrowness of the peaks. The prior volume is limited to $[0, 10\pi]$, and a fine grid integration gives $\ln \mathcal{Z} = 235.856$, which will be used as the true value. We use the same setup as in §4.1.

Sampler performance (see Table 3), for the ladder adaptation methods, the SAR and SMD methods rank best at 5.79 ± 0.29 and 5.66 ± 0.23 kenits with overlapping uncertainties, followed closely by the other methods. Out of the DNS methods, dyn-rs has the lowest wall-time, as well as the highest kenits count 0.82 ± 0.07 , 14.2% of the SAR kenits count.

Evidence estimation, the TI algorithm misses the mark by $\Delta_{\mathcal{Z}}=11.53\%$, with the worst overall likelihood $\mathcal{L}(\hat{\mathcal{Z}})=-0.643$. The TI+ improves this to $\Delta_{\mathcal{Z}}=1.43\%$, with a likelihood ratio of $\exp(2.658 - (-0.643)) = 26.87$. The

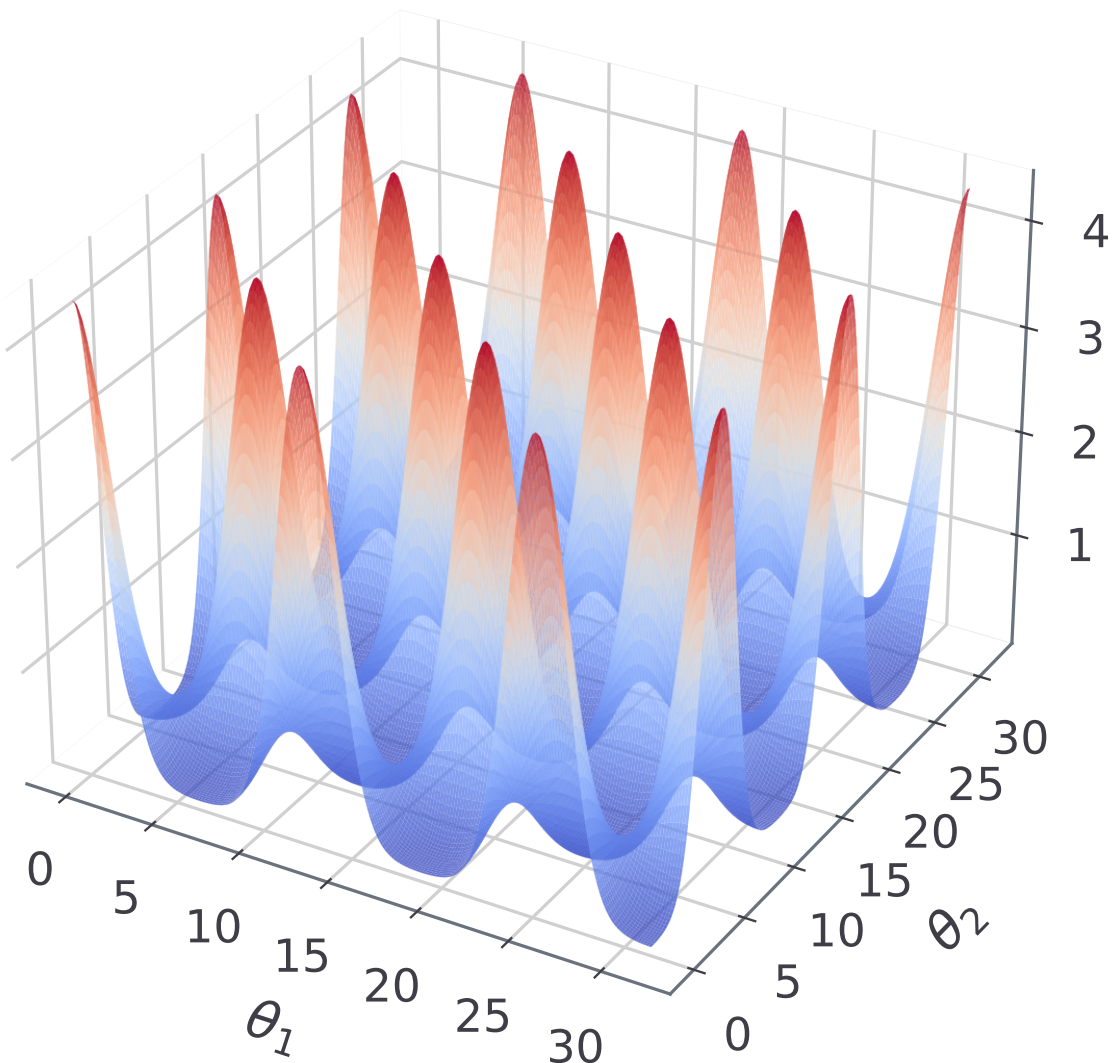


Figure 2: Gaussian Egg-box likelihood, with 16 different modes. Likelihood values are coloured from blue (low) to red (high) to facilitate visualisation.

Table 3: Egg-box performance benchmark. `reddemcee`'s adaptive algorithms compared to `dynesty`'s sampling methods. From left to right: Time–total run time in seconds, Eff–sampling efficiency or percentage of independent samples, and Kenits–effective samples per second in thousands.

Method	Time (s)	Eff (%)	Kenits
SAR	22.90±0.11	8.10±0.43	5.79±0.29
SMD	23.02±0.24	7.95±0.32	5.66±0.23
SGG	23.35±0.14	7.69±0.28	5.40±0.19
GAO	23.36±0.24	7.84±0.30	5.50±0.20
ETL	23.52±0.26	7.90±0.38	5.51±0.28
dyn-u	30.41±1.51	10.71±0.88	0.45±0.02
dyn-s	19.83±0.79	3.06±0.22	0.69±0.03
dyn-rs	16.87±1.50	3.21±0.39	0.82±0.07

Table 4: Egg-box evidence SAR estimation comparison. `reddemcee`'s adaptive algorithms compared to `dynesty`'s sampling methods. From left to right, the log-evidence estimate, the estimate error, the difference to the true value $\ln \mathcal{Z}=235.856$ in percentage $\Delta_{\mathcal{Z}}$, and the log-likelihood of the estimator $\mathcal{L}(\hat{\mathcal{Z}})$.

	$\ln \hat{\mathcal{Z}}$	$\hat{\sigma}_{\ln \hat{\mathcal{Z}}}$	$\Delta_{\mathcal{Z}}(\%)$	$\mathcal{L}(\hat{\mathcal{Z}})$
TI	235.733±0.013	0.748±0.008	11.532	-0.643
SS	235.843±0.012	0.008±0.001	1.252	2.618
H	235.802±0.013	0.130±0.006	5.283	1.036
TI+	235.842±0.013	0.023±0.008	1.425	2.648
SS+	235.844±0.013	0.008±0.001	1.211	2.771
H+	235.845±0.013	0.010±0.003	1.099	3.082
dyn-u	235.858±0.104	0.064±0.001	0.201	1.828
dyn-s	235.903±0.104	0.064±0.001	4.812	1.560
dyn-rs	235.953±0.118	0.064±0.001	10.186	0.679

SS presents the a log-likelihood of $\mathcal{L}(\hat{\mathcal{Z}})=2.618$. It's SS+ counterpart marginally closes $\Delta_{\mathcal{Z}}$ from 1.25% to 1.21%, with $\mathcal{L}(\hat{\mathcal{Z}})=2.771$. The H+ method performs better than either SS+ or TI+, at $\mathcal{L}(\hat{\mathcal{Z}})=1.099$, with $\mathcal{L}(\hat{\mathcal{Z}})=3.082$. Out of the DNS methods, dyn-u finds all modes (extremely accurate $\Delta_{\mathcal{Z}}=0.201$) at the cost of many likelihood calls. Meanwhile, slice-based samplers are faster but slightly undersampled some modes (evidence biases). dyn-u has the highest log-likelihood out of DNS methods, at 1.828. Against H+, it gives a ratio of $\exp(3.082 - 1.828) = 3.5$, almost four times as likely.

4.3 Hybrid Rosenbrock Function

The Rosenbrock function is a long, thin, curved valley with strong non-linear correlations, slightly resembling a banana. The hybrid-Rosenbrock function is an extension that provides analytic evidence for any dimension [46]. Its likelihood is defined by:

$$p(\vec{x}) = -a(x_1 - \mu)^2 - \sum_{j=1}^{n_2} \sum_{i=2}^{n_1} b_{j,i}(x_{j,i} - x_{j,i-1}^2)^2 \quad (27)$$

Where $x_{j,i}, \mu \in \mathbb{R}$, and $a, b_{j,i} \in \mathbb{R}^+$ are arbitrary constants. Its evidence is given by:

$$\mathcal{Z} = \sqrt{\frac{\pi^n}{a \cdot \prod b_{j,i}}} \quad (28)$$

Where $n = (n_1 - 1)n_2 + 1$, and n_1 is the number of dimensions in each of the n_2 groups. Per [16], a scale factor of 1/20 is chosen, with $a = 1/20$ and all $b_{j,i} = 100/20$, so the distribution is shaped like a narrow ridge, providing a challenging posterior shape (see Fig. 3).

Studying first the 2-d case, temperature evolution will be assessed, so the APT setup is changed to [24, 120, 1024, 1], increasing the number of temperatures to 24 and the sweeps to 1024, while decreasing the walkers to 120, roughly maintaining the total number of iterations the same as previous benchmarks.

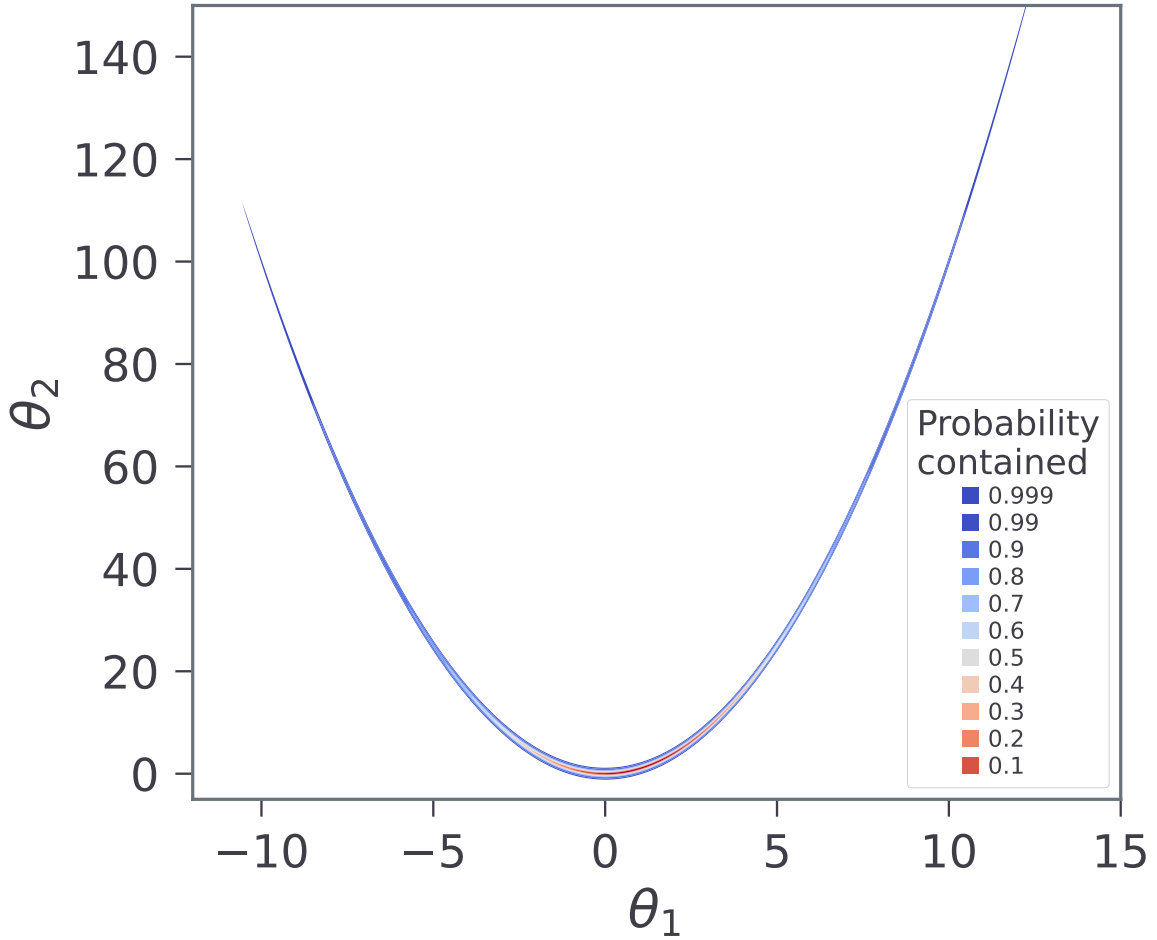


Figure 3: Probability contour of the 2-d Rosenbrock function. The inset key shows how the colours relate to the probability.

Sampler performance (see Table 5), the SAR method ranks best with 14.65 ± 0.59 kenits, followed closely by SGG, GAO, and ETL. SMD ranks last, with 6.40 ± 0.41 kenits. For the DNS methods, dyn-rs ranks first with 0.77 ± 0.02 kenits, and dyn-u ranks last with 0.34 ± 0.02 kenits, and almost twice the wall-time. In this scenario, SAR presents increased kenits over dyn-rs by a factor of 19.03, almost 20 times more efficient at producing independent samples.

Evidence estimation, the H+ method relies completely on SS+, dropping TI+ segments (see Table 6). This can be attested by the poor TI+ performance compared to SS+. The slice-sampling methods present negative log-likelihoods, indicating substantially underestimated errors.

A 3-d case for the Rosenbrock function was also explored (results discussed in Section 6); generally the trends held, with `reddemcee` outperforming in sampling efficiency, and all ladder methods producing accurate evidences (see Table 11).

5 Exoplanet detection from Radial Velocities

An real-world application of the APT ladder dynamics developed in Section 3, as well as the evidence estimation methods introduced in Section 2.4 is presented for the nearby G-dwarf HD 20794. Hosting at least three super-Earths whose RV semi-amplitudes are lower than 1 ms^{-1} , the system combines low amplitudes, multiplicity and a long-period planet, all features that make model selection and evidence estimation particularly demanding. The innermost

Table 5: 2-d Hybrid Rosenbrock performance benchmark. `reddemcee`'s adaptive algorithms compared to `dynesty`'s sampling methods with the 2-d Hybrid Rosenbrock function. From left to right: Time–total run time in seconds, Eff–sampling efficiency or percentage of independent samples, and Kenits–effective samples per second in thousands.

Method	Time (s)	Eff (%)	Kenits
SAR	19.15±0.20	9.51±0.38	14.65±0.59
SMD	19.14±0.14	4.15±0.28	6.40±0.41
SGG	19.44±0.26	9.03±0.53	13.70±0.69
GAO	19.41±0.13	8.89±0.48	13.51±0.74
ETL	19.59±0.18	9.04±0.50	13.61±0.83
dyn-u	38.28±2.85	8.04±0.81	0.34±0.02
dyn-s	21.74±0.93	2.18±0.06	0.59±0.03
dyn-rs	16.52±0.42	2.72±0.09	0.77±0.02

Table 6: 2-d Hybrid Rosenbrock SAR evidence estimation comparison. `reddemcee`'s adaptive algorithms compared to `dynesty`'s uniform (dyn-u), slice(dyn-s), and random-slice (dyn-rs) sampling methods. From left to right, the log-evidence estimate, the estimate uncertainty, the difference to the true value $\ln \mathcal{Z}=1.838$ in percentage $\Delta_{\mathcal{Z}}$, and the log-likelihood of the estimator $\mathcal{L}(\hat{\mathcal{Z}})$.

Method	$\ln \hat{\mathcal{Z}}$	$\hat{\sigma}_{\ln \hat{\mathcal{Z}}}$	$\Delta_{\mathcal{Z}}(\%)$	$\ln \mathcal{L}_{\hat{\mathcal{Z}}}$
TI	1.416±0.022	0.912±0.025	34.431	-0.934
SS	1.833±0.020	0.011±0.001	0.515	3.479
H	1.833±0.020	0.011±0.001	0.515	3.479
TI+	1.781±0.022	0.227±0.017	5.565	0.531
SS+	1.833±0.022	0.012±0.001	0.515	3.399
H+	1.833±0.022	0.012±0.001	0.515	3.399
dyn-u	1.881±0.089	0.076±0.001	4.394	1.501
dyn-s	2.007±0.221	0.074±0.004	18.412	-0.936
dyn-rs	1.979±0.164	0.074±0.002	15.258	-0.144

signals at 18 and 90 days were first identified in the HARPS discovery paper [47], while subsequent analyses revealed an outer candidate with a period of ~ 650 d that spends a significant fraction of its eccentric orbit inside the stellar habitable zone [48].

As such, this system provides an ideal test-bed for assessing the performance and proposed evidence estimation algorithms in a real-world example. In this section, the work by [48] is followed, applying `reddemcee` to the combined HARPS+ESPRESSO time-series, contrasting the resulting evidences with those reported in the literature.

5.1 Model and Likelihood

Each exoplanet, or Keplerian signal, is characterised by five parameters, P –the period, K –the semi-amplitude, e –the eccentricity, $\bar{\omega}$ –the longitude of periastron, and T_0 –time of periastron passage:

$$\mathcal{K}_j(t) = K_j \cdot [\cos(\nu_j(t, P_j, e_j, T_0) + \bar{\omega}_j) + e_j \cos(\bar{\omega}_j)] \quad (29)$$

Where the sub-index j indicates each exoplanet and ν_j is the true anomaly. In addition, each different instrument is given an offset γ (an additive constant) and a jitter σ_{INS} (added in quadrature to the measurement error, corresponding to a white noise component). Therefore, under the assumption of Gaussian-like errors, the log-likelihood is given by:

$$\ln \mathcal{L} = -\frac{1}{2} \sum_{\text{INS}} \sum_i^{N_{\text{INS}}} \left(\frac{\xi_{i,\text{INS}}^2}{(\sigma_i^2 + \sigma_{\text{INS}}^2)} + \ln(\sigma_i^2 + \sigma_{\text{INS}}^2) \right) - \frac{N \ln(2\pi)}{2} \quad (30)$$

Table 7: HD 20794 evidence estimation comparison. Difference of the model’s mean evidence with the evidence of the best ranking model. The models shown from top to bottom are, white noise only (H_0), increasing sinusoids (S), and increasing Keplerians (K). The reference evidences have an offset added to make the H_0 evidence equivalent to the SAR. (1) [48]; (2) unreported standard deviation.

Model	Reference ¹	dyn-rs	SAR
H_0	-111.9±0.2	-111.2±0.1	-111.9±0.1
1 S	-72.9±3.0	-65.1±2.7	-64.2±0.1
2 S	-41.7±3.7	-40.2±2.4	-40.2±0.2
3 S	-12.3±2.0	-16.0±1.1	-11.5±0.1
3 K	-3.6±0.0 ²	-12.9±2.6	-5.8±0.5
4 K	-1.6±4.6	-4.6±3.8	0.0±1.0

Table 8: HD 20794 evidence estimation uncertainty and performance. Left columns show the ratio of the mean of the estimated evidence uncertainty against the standard deviation of the run-to-run evidence. Right columns, the average kenits, with the efficiency in parenthesis. The models are white noise only (H_0), increasing sinusoids (S), and increasing Keplerians (K). (1) [48].

Model	$\frac{\hat{\sigma}_{\ln \hat{\mathcal{Z}}}}{\sqrt{\text{Var}[\ln \hat{\mathcal{Z}}]}}$		kenits (eff)	
	dyn-rs	SAR	dyn-rs	SAR
H_0	2.30	11.4	0.375 (2.5)	0.889 (7.8)
1 S	0.05	0.48	0.193 (1.3)	0.679 (4.7)
2 S	0.07	0.75	0.120 (1.0)	0.242 (1.9)
3 S	0.12	2.03	0.097 (0.8)	0.207 (1.7)
3 K	0.07	0.63	0.051 (0.5)	0.046 (0.4)
4 K	0.04	0.27	0.039 (0.5)	0.030 (0.3)

where the sub-indices i and INS correspond to the i -th RV measurement (taken at a time t_i) and to each instrument, respectively. The residuals $\xi_{i,\text{INS}}$ are defined as the difference between the data and the model. Three distinct datasets plus three Keplerian signals add up to a total of 21 parameters or dimensions.

5.2 Parameter Estimation and Model Selection

For an in-depth methodology follow up, refer to [Appendix 10](#). The models compared are 1) just white noise (H_0), 2) a single sinusoid (1S), 3) two sinusoids (2S), 4) three sinusoids (3S), 5) 3 Keplerians (3K), and 6) 4 Keplerians (4K). Sinusoids models (S) treat planets as having circular orbits. The 3K model corresponds to the three confirmed planets, and 4K to an additional candidate.

For the evidence estimation (see [Table 7](#)), dyn-rs was consistent with the SAR, up to the most complex models. For the 3S, 3K, and 4K models, they had a 4.6, 6.8, and 4.6 $\ln \hat{\mathcal{Z}}$ difference. On the other hand, the SAR log-evidences were consistent with the reference values within their uncertainties, except 1S, showing a moderate discrepancy (~ 8.7). This could be due random variation or differences in how jitter/noise was treated, but importantly the model ranking is unaffected.

[Table 8](#) compares the estimated evidence errors to the actual run-to-run scatter (the ratio $\hat{\sigma}_{\mathcal{Z},\text{estimated}}/\hat{\sigma}_{\mathcal{Z},\text{empirical}}$). An ideal ratio is 1. Values $\ll 1$ mean the method underestimates its true uncertainty, and $\gg 1$ means overestimation. The dyn-rs ratios are all very low for complex models (0.04-0.12), severely underestimating the uncertainty with overly confident evidences, whereas `reddemcee` presents values much closer to unity (0.63 for the 3K). Underestimation of the error in multi-planet cases could risk overconfident claims of detection, therefore `reddemcee` (with the H+ estimator) provides more conservative and reliable uncertainties.

Performance-wise, APT achieves higher kenits count in the simpler models, with a turn-over point at 3K in favour of dyn-rs. This may be attributed to the modest fixed amount of walkers (256) in the APT sampler (more details in [Appendix 10](#)). In practice, one could adjust walker count for efficiency’s sake, but it was kept constant for consistency.

Table 9: HD 20794 parameter estimation. Parameter estimation results for the different algorithms for the 3K model. In descending order, P corresponds to the period, K to the semi-amplitude, and e to the eccentricity, where the sub-index denotes a particular planet. (1) [48].

Parameter	Reference ¹	dyn-rs	SAR
P_1 (days)	18.314 ± 0.002	$18.314^{+0.004}_{-0.004}$	$18.313^{+0.001}_{-0.001}$
K_1 (ms^{-1})	0.614 ± 0.048	$0.632^{+0.030}_{-0.066}$	$0.608^{+0.030}_{-0.009}$
e_1	$0.064^{+0.065}_{-0.046}$	$0.109^{+0.049}_{-0.068}$	$0.057^{+0.045}_{-0.057}$
P_2 (days)	89.68 ± 0.10	$89.67^{+0.11}_{-0.16}$	$89.73^{+0.06}_{-0.03}$
K_2 (ms^{-1})	$0.502^{+0.048}_{-0.049}$	$0.510^{+0.038}_{-0.054}$	$0.474^{+0.041}_{-0.001}$
e_2	$0.077^{+0.084}_{-0.055}$	$0.055^{+0.053}_{-0.054}$	$0.026^{+0.007}_{-0.026}$
P_3 (days)	$647.6^{+2.5}_{-2.7}$	$652.1^{+4.5}_{-5.5}$	$648.2^{+2.6}_{-2.4}$
K_3 (ms^{-1})	$0.567^{+0.067}_{-0.064}$	$0.521^{+0.025}_{-0.091}$	$0.589^{+0.001}_{-0.055}$
e_3	$0.45^{+0.11}_{-0.10}$	$0.428^{+0.111}_{-0.412}$	$0.467^{+0.053}_{-0.024}$

For the parameter estimation, both methods give consistent results between them (see Table 9). Notably, the APT parameter estimates are slightly more asymmetrical and tight (see K_2 and K_3). Also, the eccentricity estimates seem less adverse to the boundary solutions, as seen in $e_1=0.057^{+0.045}_{-0.057}$ and $e_2=0.026^{+0.007}_{-0.026}$, both consistent with $e = 0$.

6 Discussion

The evidence estimation algorithms introduced in Section 2.4 have proven to be far more reliable than their unmodified counterparts. Furthermore, whether to apply the TI or the SS method is mostly problem-dependent, and the hybrid algorithm seems a good compromise when there is no a priori information on the problem at hand. Moreover, our proposed evidence estimators provide a solid alternative, if not better, to dedicated evidence algorithms like DNS. This is exemplified by the real-world case studied in Section 5.

Across the simplest problems we tested (few dimensions, nearly constant specific heat), all ladder strategies converge to an almost geometric ladder and yield similar performance. Differences emerge as the problem's complexity grows, and since a common problem astrophysicists face is that of dimensionality, we further discuss it next.

6.1 Increasing Dimensionality

We take the Gaussian Shells problem described in §4.1 and increase the dimensionality, without modifying any of the hyper-parameters of the initial setup (same chain-length). As we increase dimensions, we see a very much expected decrease in efficiency (see Table 10), as well as the SMD outperforming other methods. At 15 dimensions, it becomes the most effective, with a margin far exceeding the run-to-run scatter. In second place, GAO and ETL come tied (with overlapping confidence intervals), being around 14% slower, followed by the SAR—at 19% slower—and the SGG—being 34% slower. This supports the intuition that maximising swap distance is beneficial in high dimensional spaces where local energy traps abound. On the other hand, dyn-rs, still the best DNS method, presents kenits at $\sim 13\%$ of the SMD average.

For evidence estimation, with the modest amount of temperatures proposed for this benchmark, the TI method degrades considerably, with a $\Delta_{\mathcal{Z}}$ of $\sim 72\%$ (see Table 12). The TI+ soothes this, with a $\Delta_{\mathcal{Z}} 11.3\%$. Nevertheless, the error due the discretisation remains a problem in this benchmark. For the SS method, the evidence estimate is excellent ($\Delta_{\mathcal{Z}}=2.56$), with the highest $\mathcal{L}(\hat{\mathcal{Z}})=2.1658$. The SS+ method presents a slight deterioration over its classic counterpart. The H+ presents a higher likelihood (and lower $\Delta_{\mathcal{Z}}$) than either TI+ or SS+.

By increasing the dimensionality of the Rosenbrock function to 3-d, the evidence estimation results (H+) are best for ETL with $\mathcal{L}(\hat{\mathcal{Z}})=2.901$, followed by SGG and GAO, with $\mathcal{L}(\hat{\mathcal{Z}})=1.841$ and 1.561 , respectively (see Table 11). The kenits values present a similar trend to that of the shells, with 2.98 (SAR), 2.50 (SMD), 3.46 (SGG), 3.03 (GAO), and 2.85 (ETL); and 0.02 (dyn-u), 0.55 (dyn-s), and 0.74 (dyn-rs).

Table 10: Gaussian Shells with increasing dimensions performance. `reddemcee`'s adaptive algorithms compared to `dynesty`'s sampling methods. The Kenits—effective samples per second in thousands—are shown, from left to right we have increasing dimensions from 2 to 15.

Method	2-d	5-d	10-d	15-d
SAR	3.70±0.12	3.59±0.12	2.71±0.11	2.25±0.07
SMD	3.73±0.13	3.73±0.14	3.21±0.14	2.80±0.09
SGG	3.67±0.13	3.50±0.11	2.45±0.07	1.85±0.07
GAO	3.60±0.11	3.61±0.15	2.84±0.07	2.36±0.07
ETL	3.66±0.10	3.66±0.12	2.89±0.07	2.45±0.13
dyn-u	0.19±0.04	0.37±0.04	0.32±0.05	0.18±0.01
dyn-s	0.75±0.04	0.43±0.01	0.23±0.01	0.17±0.01
dyn-rs	0.94±0.05	0.70±0.01	0.46±0.01	0.37±0.01

Table 11: Hybrid 3-d Rosenbrock evidence estimation. `reddemcee`'s adaptive algorithms compared to `dynesty`'s sampling methods. From left to right, the log-evidence estimate, the estimate error, the difference to the true value $\ln \mathcal{Z}=1.606$ in percentage in percentage $\Delta_{\mathcal{Z}}$, and the log-likelihood of the estimator $\ln \mathcal{L}(\hat{\mathcal{Z}})$.

Method	$\ln \hat{\mathcal{Z}}$	$\hat{\sigma}_{\ln \hat{\mathcal{Z}}}$	$\Delta_{\mathcal{Z}}$	$\ln \mathcal{L}(\hat{\mathcal{Z}})$
SAR	1.562±0.062	0.021±0.001	4.233	0.771
SMD	1.516±0.065	0.023±0.002	8.519	-4.556
SGG	1.574±0.076	0.021±0.002	3.069	1.841
GAO	1.570±0.042	0.022±0.002	3.500	1.561
ETL	1.598±0.061	0.021±0.001	0.747	2.901
dyn-u	1.923±0.207	0.109±0.002	37.366	-2.944
dyn-s	1.625±0.883	0.111±0.004	1.967	1.264
dyn-rs	1.534±0.442	0.112±0.006	6.903	1.066

6.2 Burn-in

How fast the adaptation distributes the ladder optimally depends on the both the problem at hand and the adaptation hyper-parameters ν_0, τ_0 . We stress test the adaptation by setting the 15-d shells with 640 sweeps (as in §4.2 and §6.1) to use 320, 160, 64, and 32 sweeps as burn-in (see Table 13). H+ is the method most resilient to an un-calibrated ladder, it's the only method that retains positive $\mathcal{L}(\hat{\mathcal{Z}})$ values after the 25% burn-in, with values $\ln \hat{\mathcal{Z}}|_{H+}=-24.939\pm 0.037$, -24.980 ± 0.031 , -24.984 ± 0.034 , and -24.996 ± 0.041 , for 50%, 25%, 10%, and 5%, respectively.

6.3 Ladder Adaptation

For low-dimensional targets (2-d shells, egg-box) every method settles on an almost geometric ladder, due to $C_v(\beta)$ being almost flat. As the dimensionality grows, C_v develops a broad peak around the phase-transition region, and the objectives react differently. For example, the SAR spreads the temperatures uniformly in swap probability and therefore stretches the ladder on both sides of the peak, while SMD concentrates the replicas where the specific heat is large, maximising the average information transfer, as seen by its clear lead at 15-d in Table 10.

Longer runs are realised for this scenario, 15-d shells, with 10 000 sweeps instead of 640, to examine the convergence of the ladder adaptation. All schemes compress the first ~ 200 sweeps into a fast logistic-like relaxation of the temperature gaps, after which the diminishing adaptive factor $\kappa(t)$ (Eq.14) forces a slow power-law tail. In practice, almost the whole ladder shape is set in under 5% of the computational budget, supporting the choice of freezing the ladder after a user-defined burn-in.

Figures 4 and 5 display the ladder evolution of the SAR and SMD methods, respectively. A notable difference is that the SMD method has a layered swap rate, where the cold chain swaps frequently (0.7), and the hot chain seldom (0.2), whereas the SAR keeps a steady swap rate of 0.5 for all temperatures.

Fig.6 shows the final ladders as chain density (proportional to C_v) as a function of temperature. The dashed vertical lines indicate where $\Delta\beta$ is smaller, as well as where the transition between TI and SS is applied in the hybrid method.

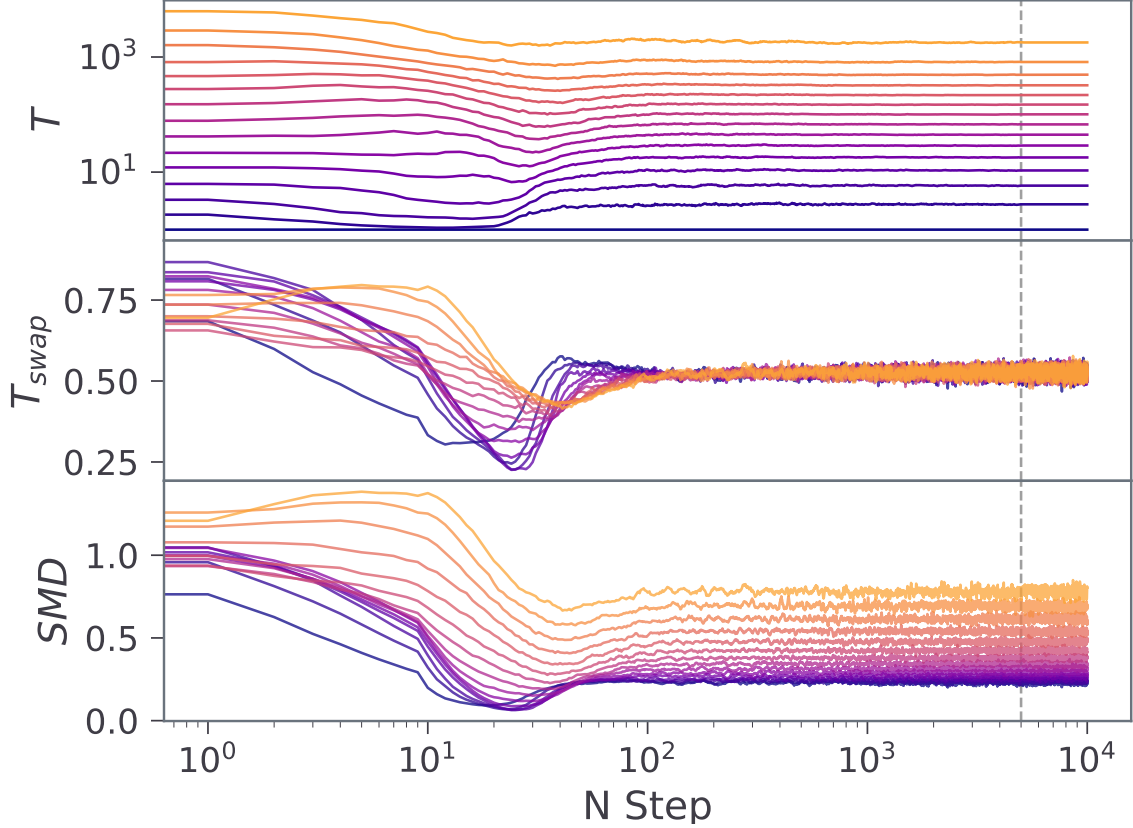


Figure 4: SAR ladder evolution for the 15-d Gaussian shells. In the x-axis is the current iteration, and from top to bottom, the current temperature ladder T , the swap acceptance ratio T_{swap} , and the swap mean distance SMD. Colours represent each chain, where blue is the coldest ($\beta=1$), with increasing temperature to the red, where the hottest chain is omitted. The vertical black dashed line indicates where the adaptation stops.

6.4 Number of Temperatures

A natural question that arises is ‘how many temperatures are enough?’ The answer, as one might expect, is ‘it depends’. When doing an APT run, there are two objectives in mind, posterior and evidence estimation. More temperatures might be redundant posterior wise, not contributing with additional information to the cold chain. At the same time, more temperatures provide a finer grid for the evidence estimation. Nonetheless, it is possible to dabble into this question, by analysing the temperature evolution of the ladder. If the mixing is low, increasing the temperatures will result in a more efficient run. This may be measured by comparing the additional chains computational cost against the efficiency (or kenits) increase. Visualising the likelihood variance as a function of temperature (the thermodynamic integration) can be helpful. A smoothly increasing curve will not be affected as much as a ladder-like curve by decreasing temperatures. This can also be appreciated by the C_v plot, a ladder-like behaviour would be seen as multiple sharp peaks (as in the HD 20794 3K model, see Fig.7, with a secondary small peak at around $\beta=0.4$), whereas a smooth curve is seen as a single smooth peak (like in the 15-d shells, see Fig.6).

But how are the different evidence estimation algorithms proposed affected? The 15-d shells (with 10 000 sweeps) is re-run with $N_\beta=6, 8, 12$, and 16 (see Table 14).

The TI method by decreasing temperatures, presents a linear fall-off with $\sqrt{\mathcal{L}_{\hat{\mathcal{Z}}}}$, this result can also be easily derived from Eq.8, which will reveal that the log-evidence error is proportional to $\frac{1}{n_{\text{temps}}}$. The TI+ method presents a huge improvement over TI, although still failing to reach the mark in temperature poor regimes. The SS methods remain extremely accurate even at low $N_\beta = 6$, with $\Delta_{\mathcal{Z}}=1.78$ and $\mathcal{L}(\hat{\mathcal{Z}})=2.02$. The geometrical bridge in SS+ yields a small

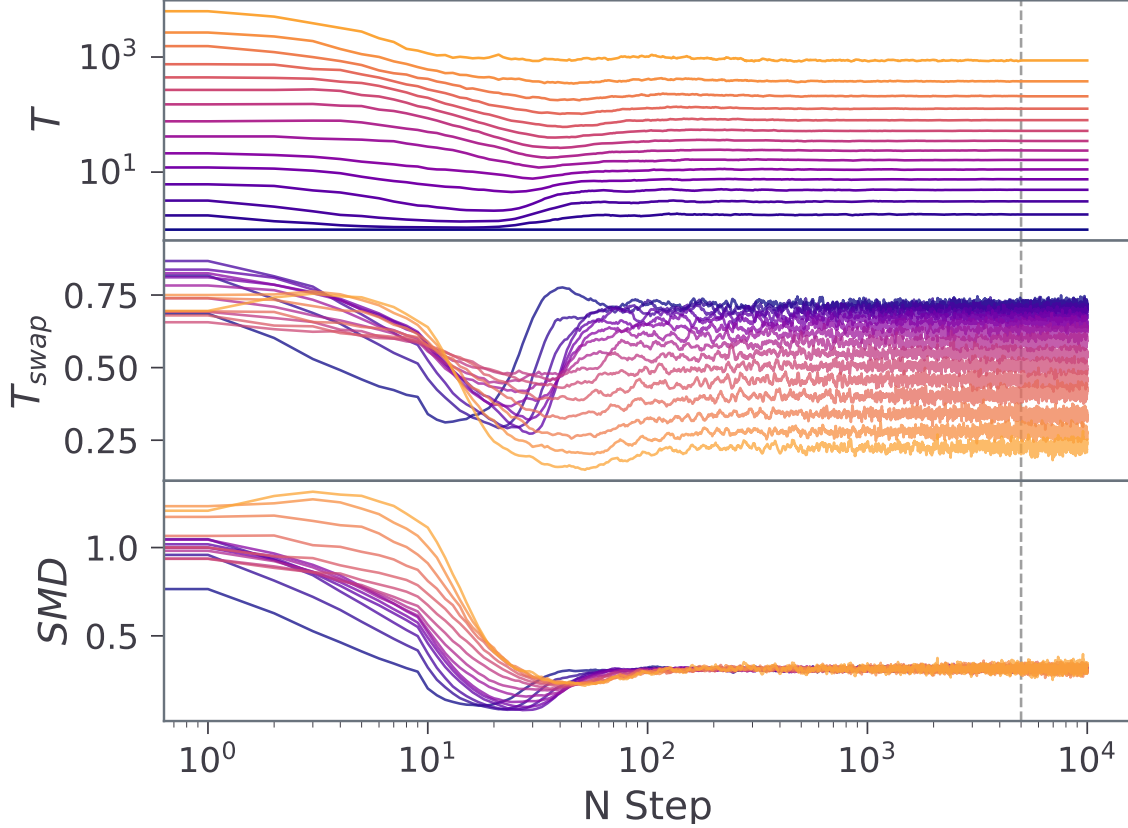


Figure 5: SMD ladder evolution for the 15-d Gaussian shells. In the x-axis is the current iteration. Descending, the temperature ladder evolution T , the swap acceptance ratio T_{swap} , and the swap mean distance SMD. Colours represent each chain, where blue is the coldest ($\beta=1$), with increasing temperature to the red, where the hottest chain is omitted. The vertical black dashed line indicates where the adaptation stops.

accuracy gain (lower $\Delta_{\mathcal{Z}}$ for every N_{β}), while bringing a small drop in $\mathcal{L}(\hat{\mathcal{Z}})$, due the slight increase in the error estimate.

7 Conclusions

We have introduced `reddemcee`, an Adaptive Parallel Tempering ensemble sampler that couples three next-level techniques—flexible ladder adaptation, robust evidence estimation, and practical error quantification—into a single, easy-to-deploy package. Three of the five ladder adaptation algorithms are new implementations from this work (SMD, SGG, ETL), reliable alternatives to the most commonly used SAR method, as demonstrated in our benchmarks (see Section 4). All of these methods converge in a few sweeps and deliver cold-chain mixing efficiencies around an order of magnitude higher than dynamic nested sampling across our tests. In the challenging 15-d Gaussian-shell benchmark, `reddemcee` sustained > 2 kenits, about 7 times faster than the best DNS configuration, while the SMD ladder proved particularly resilient as dimensionality grew.

We devised three evidence estimators—two original implementations, TI+ and SS+, and a novel hybrid approach—that combine curvature-aware interpolation with bridge sampling. These estimators yield accurate log-evidences and maintain realistic uncertainties even when the number of temperatures is decreased beyond optimal.

A real-world application to the HD 20794 radial-velocity dataset shows that `reddemcee` reproduces literature model rankings, recovers planetary parameters with tighter—yet statistically consistent—credible intervals, and supplies evidence uncertainty that closely tracks run-to-run dispersion. Crucially, this performance is obtained without manual

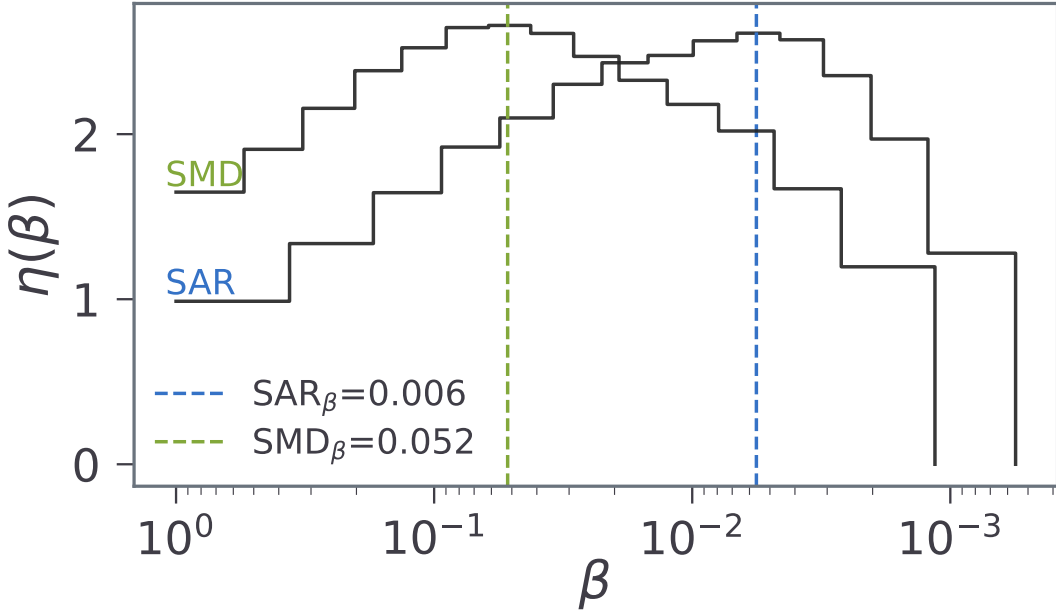


Figure 6: Chain density per temperature range for the SAR and SMD methods in the 15-d Gaussian shells. The blue dashed line denotes the maximum of the SAR, with the green one representing the maximum of the SMD. Both lines also denote the regions where the TI or SS algorithms are applied in the Hybrid method.

ladder tuning: the same hyper-parameters were used from no-planet to four-planet models and from 6 to 21 dimensions.

Overall, `reddemcee` demonstrates that a carefully engineered APT sampler can match, and occasionally surpass, state-of-the-art DNS, both in sampling throughput and in evidence estimation, while retaining the posterior-inference strengths that make MCMC indispensable. Future work will explore on-the-fly convergence diagnostics, further widening the sampler’s applicability to the increasingly complex problems faced in modern astrophysics and beyond.

8 Acknowledgements

PAPR and JSJ gratefully acknowledge support by FONDECYT grant 1240738 and from the ANID BASAL project FB210003. For the n-d Gaussian Shells, Gaussian Egg-box, and Rosenbrock Function benchmarks parallelisation was not used and computing was limited to single-core for all algorithms. For the exoplanet detection benchmark, parallelisation was used with 24 threads. All the benchmarks were performed on a computer with an *AMD Ryzen Threadripper 3990X 64-Core Processor* with 128Gb of DDR4 3200Mhz RAM. We are grateful to Fabo Feng and Mikko Tuomi for stimulating early discussions on planet detection. We would also like to thank Dan Foreman-Mackey for the excellent library `emcee` [49], which opened a most exciting new world. Typesetting was carried out in `Overleaf` [50].

9 Appendix A–Gaussian Shells

10 Appendix B–HD 20794

Each dataset, HARPS03, HARPS15, and E19, is nightly binned, then sigma clipped (3σ), and excluded of measurements where the error is higher than 3 times the median error for that dataset, leaving out 512, 231, and 63 RVs respectively, for a grand-total of 806 RVs. Priors were matched to those stated by [48], with unspecified priors left to an educated guess. For offset a prior $\sim \mathcal{U}(-3, 3)$ was chosen, and for jitter $\sim \mathcal{N}(0, 5)$, truncated at $[0, 3]$. By com-

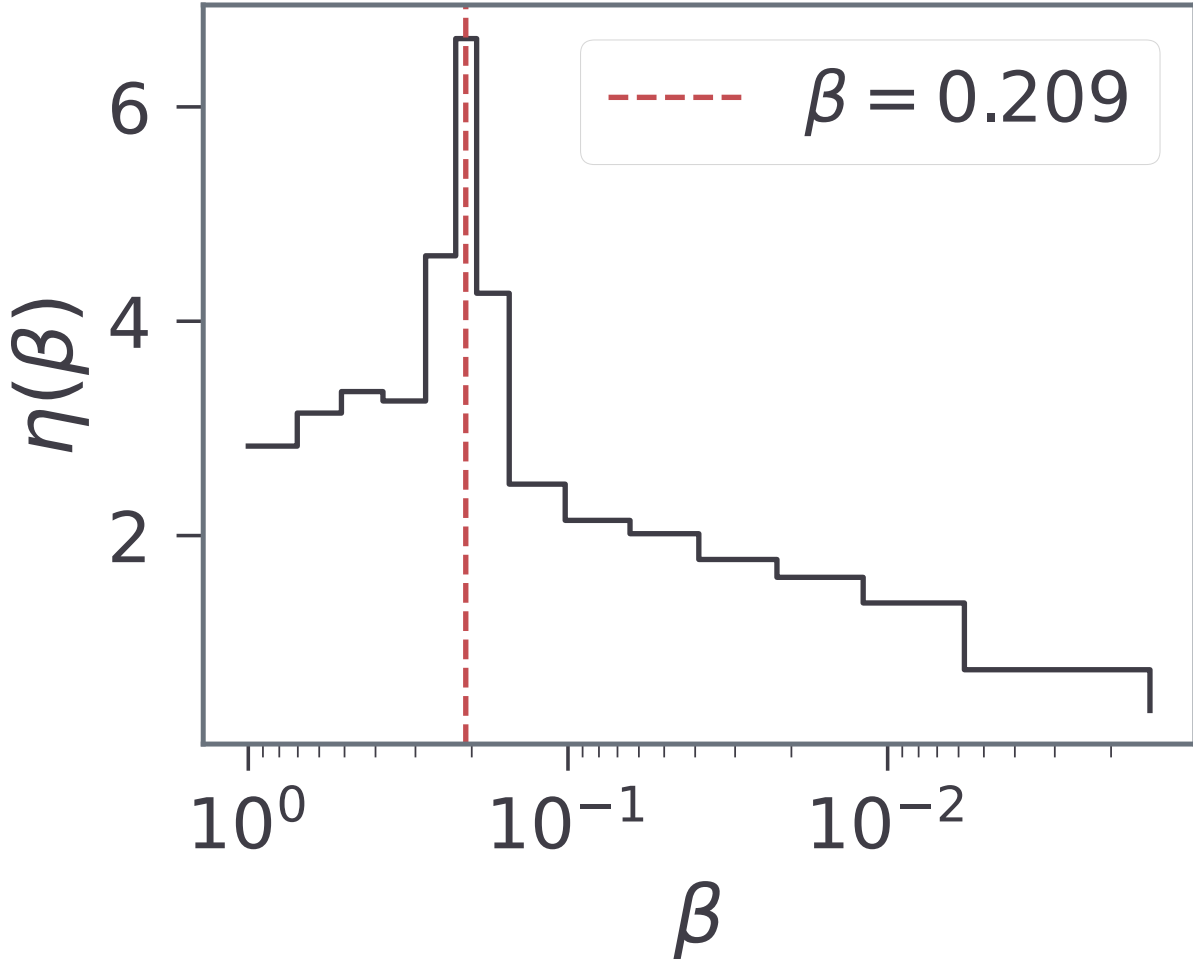


Figure 7: Chain density per temperature range for the HD20794 3K SAR run. The vertical dashed red line marks the distribution maximum, shown in the plot key.

Table 12: 15-d Gaussian Shells evidence estimation comparison with the SAR method. `reddemcee`'s adaptive algorithms compared to `dynesty`'s sampling methods. From left to right, the log-evidence estimate, the estimate uncertainty, the difference to the true value $\ln \mathcal{Z} = -24.9114$ in percentage $\Delta_{\mathcal{Z}}$, and the log-likelihood of the estimator $\mathcal{L}(\hat{\mathcal{Z}})$.

Method	$\ln \hat{\mathcal{Z}}$	$\hat{\sigma}_{\ln \hat{\mathcal{Z}}}$	$\Delta_{\mathcal{Z}}$	$\mathcal{L}(\hat{\mathcal{Z}})$
TI	-26.1818±0.0417	1.1037±0.0526	71.9266	-1.6800
SS	-24.9374±0.0410	0.0205±0.0029	2.5617	2.1658
Hybrid	-24.9523±0.0423	2.9866±0.0661	4.0070	-2.0132
TI+	-25.0308±0.0375	0.5979±0.0266	11.2557	-0.4245
SS+	-24.9411±0.0369	0.0204±0.0021	2.9299	1.9090
Hybrid+	-24.9394±0.0373	0.0242±0.0027	2.7599	2.1337
dyn-u	-24.7176±0.3144	0.1246±0.0017	21.3853	-0.0460
dyn-s	-24.8765±0.3044	0.1243±0.0015	3.5620	1.1267
dyn-rs	-24.7292±0.2163	0.1242±0.0012	19.9854	0.0908

paring the differences between the best solution of each model, our dyn-rs results match with the reference only for

Table 13: 15-d Gaussian Shells $\ln \mathcal{Z}$ estimation with variable burn-in for the SAR method. `reddemcee`'s SAR method evidence estimation with different adaptation (and burn-in) times, starting at half of the chain $N_{\text{adapt}}=50\%$, down to 25%, 10%, and 5% for 640 sweeps. Each sub-column shows the difference to the true value $\ln \mathcal{Z}=-24.9114$ in percentage $\Delta_{\mathcal{Z}}$, and the log-likelihood of the estimator $\mathcal{L}(\hat{\mathcal{Z}})$.

Method	$N_{\text{adapt}}=50\%$		$N_{\text{adapt}}=25\%$		$N_{\text{adapt}}=10\%$		$N_{\text{adapt}}=5\%$	
	$\Delta_{\mathcal{Z}}$	$\mathcal{L}(\hat{\mathcal{Z}})$	$\Delta_{\mathcal{Z}}$	$\mathcal{L}(\hat{\mathcal{Z}})$	$\Delta_{\mathcal{Z}}$	$\mathcal{L}(\hat{\mathcal{Z}})$	$\Delta_{\mathcal{Z}}$	$\mathcal{L}(\hat{\mathcal{Z}})$
TI	71.9266	-1.6800	72.9348	-1.6919	71.0282	-1.8322	70.176	-22.5295
SS	2.5617	2.1658	7.0111	-5.9413	6.7014	-4.9155	8.3851	-8.4817
Hybrid	4.0070	-2.0132	21.8509	-1.4656	27.8067	-1.0694	17.2876	-2.0419
TI+	11.2557	-0.4245	14.1321	-0.5039	12.6212	-0.3977	12.3431	-0.3729
SS+	2.9299	1.9090	6.3493	-4.2133	6.3843	-4.7487	8.1264	-8.5345
Hybrid+	2.7599	2.1337	6.6707	1.2514	6.9972	1.0890	8.1322	0.9562

Table 14: 15-d Gaussian Shells $\ln \mathcal{Z}$ estimation with variable temperatures for the SAR method. `reddemcee`'s SAR method evidence estimation with $N_{\beta}=16, 12, 8$, and 6 temperatures. Each sub-column shows the difference to the true value $\ln \mathcal{Z}=-24.9114$ in percentage $\Delta_{\mathcal{Z}}$, and the log-likelihood of the estimator $\mathcal{L}(\hat{\mathcal{Z}})$.

Method	$N_{\beta}=16$		$N_{\beta}=12$		$N_{\beta}=8$		$N_{\beta}=6$	
	$\Delta_{\mathcal{Z}}$	$\mathcal{L}(\hat{\mathcal{Z}})$	$\Delta_{\mathcal{Z}}$	$\mathcal{L}(\hat{\mathcal{Z}})$	$\Delta_{\mathcal{Z}}$	$\mathcal{L}(\hat{\mathcal{Z}})$	$\Delta_{\mathcal{Z}}$	$\mathcal{L}(\hat{\mathcal{Z}})$
TI	70.7557	-1.6760	90.4453	-2.5408	99.8465	-4.0657	>100.0	-5.2445
SS	0.5806	3.6858	0.3422	4.1314	0.1161	4.1473	1.7751	2.0183
Hybrid	15.5426	-1.8808	10.6859	0.0712	18.2425	-2.7388	43.9598	-3.0542
TI+	8.6369	-0.4128	25.0197	-1.3178	77.9445	-2.5999	99.2296	-3.5185
SS+	0.5052	3.8631	0.5405	3.7914	0.0666	4.3621	1.3469	1.8170
Hybrid+	0.6942	1.8130	0.5567	1.7850	0.8203	-0.3522	8.5362	-1.6289

$\Delta\mathcal{Z}(H_0, S1)$ and $\Delta\mathcal{Z}(S1, S2)$, with diverging results by 5.3, 2.6, and -4.2 in increasing models. This could be explained by the high standard deviation (for example, for the $4K$, 4.6 and 3.8 in the reference and dyn-rs, respectively) or to differences in the sampler setup.

On the other hand, doing the same exercise against the SAR run provides much closer differences: 0.3, 2.2, -1.5, 1.6, and -0.2, with the highest values corresponding to $\Delta\mathcal{Z}(2S, 3S)$ and $\Delta\mathcal{Z}(3S, 3K)$, well within the variance.

For the `reddemcee` runs we choose an arbitrary setup of 16 temperatures, 256 walkers, and 5000 sweeps, increasing in 2500 extra sweeps for each model, with 17500 sweeps for the $4K$. This was done to facilitate the stationarity of the temperature adaptation without ‘hand-tuning’ the adaptive parameters.

The $1S$ model consistently found the $P = 18.314$ d signal, with an evidence of $\ln \hat{\mathcal{Z}}=-1217.1 \pm 0.3$, and a difference of 47.9 with the H_0 model. Adding a signal found $P_2 = 89.66$ d consistently, with an evidence improvement of 23.5. The third sinusoid shifted this period slightly to 89.7 d, whilst adding one at $P_3 = 652.2$ d, and improving the evidence by 29.1. Changing the sinusoids to Keplerians brought an improvement of 5.2 evidence-wise, with eccentricities of $e_1=0.057$, $e_2=0.026$, $e_3=0.467$. Finally, the $4K$ model brought both $P_4 \sim 1440$ d and ~ 111 d, with similar evidences and likelihoods.

The step decrease in kenits for the more complex model is attributed to the low walker count.

It is also worth noting the difference in both consistency and wall-time in these models. For $3K$ and $4K$ the standard deviation in dyn-rs was 2.6 and 3.8 respectively, compared to 0.4 and 0.9 in `reddemcee`. Furthermore, the average wall-time in dyn-rs was 150.26 ± 32.46 , and 112.77 ± 5.2 minutes, whereas in `reddemcee` it was 57.68 ± 2.57 , and 77.21 ± 2.42 minutes. Time-wise, the runs were not only significantly shorter, but also more consistent.

11 Appendix C–Evidence estimators

11.1 Geometric-Bridge Stepping Stones

For the temperature ladder $1 = \beta_1 > \dots > \beta_B \geq 0$, at each β_i we have an ensemble of W walkers evolving over T sweeps. For each adjacent pair (β_i, β_{i+1}) and for every sweep, we build a symmetric bridge [44, 45] between the two ensembles:

$$\begin{aligned} \text{from } \beta_i: \quad A_{t,i} &= \frac{1}{W} \sum_{w=1}^W \ln \mathcal{L}^{\Delta\beta_i/2} \\ \text{from } \beta_{i+1}: \quad C_{t,i} &= \frac{1}{W} \sum_{w=1}^W \ln \mathcal{L}^{-\Delta\beta_i/2} \end{aligned} \quad (31)$$

If the ladder is still adapting, we use the per-sweep $\Delta\beta_{i,t}$, otherwise (as in this manuscript) a single averaged $\Delta\beta_i$. Then we average over sweeps to get $\mu_{A,i} = \overline{A_{t,i}}$ and $\mu_{C,i} = \overline{C_{t,i}}$. Each ratio $\frac{\mu_{A,i}}{\mu_{C,i}}$ estimates r_i via the geometric bridge. Multiplying all these ratios, or adding their logs, gives the log-evidence estimate:

$$\ln \widehat{\mathcal{Z}}_{\text{SS+}} = \sum_{i=1}^{B-1} (\ln \mu_{A,i} - \ln \mu_{C,i}) \quad (32)$$

For the sampling error $\widehat{\sigma}_S^2$ we treat the per-sweep vectors $[A_{t,.} \mid C_{t,.}]$ as a correlated time series across sweeps, estimating the long-run covariance with multivariate OBM, and use the delta method for $g(\mu) = \sum_i (\ln \mu_{A,i} - \ln \mu_{C,i})$ to get $\text{Var}[\widehat{z}] = \widehat{\sigma}_S^2$ [41, 42]. This method effectively steps along the ladder with a geometric bridge at each step, propagating an autocorrelation-aware uncertainty.

11.2 Piecewise Interpolated Thermodynamic Integration

For each sweep $t = 1, \dots, T$, we take the per-temperature mean log-likelihood $\bar{\ell}_{i,t} = \frac{1}{W} \sum_{w=1}^W \ln \mathcal{L}^{\beta_i, t}$. Now, for each sweep we interpolate the curve $\mathbb{E}_\beta[U](\beta)$ with PCHIP [43], and integrate, resulting in a series \widehat{z}_t . The time-average of this series is the evidence estimate:

$$\ln \widehat{\mathcal{Z}}_{\text{TI+}} = \sum_{t=1}^T \widehat{z}_t \quad (33)$$

To estimate $\widehat{\sigma}_D$ we form a coarser ladder by dropping every other β , recompute the same PCHIP integral to get $\widehat{z}_t^{(2)}$, time-average to $\ln \widehat{\mathcal{Z}}_{\text{TI+}}^{(2)}$, and set

$$\widehat{\sigma}_D = \ln \widehat{\mathcal{Z}}_{\text{TI+}}^{(2)} - \ln \widehat{\mathcal{Z}}_{\text{TI+}} \quad (34)$$

To estimate $\widehat{\sigma}_S$, if the ladder is no longer adapting, we treat \widehat{z}_t as a correlated univariate time-series over the sweeps, estimate its long-run covariance Σ with OBM, and set $\widehat{\sigma}_S^2 = \frac{\Sigma}{T}$. Otherwise, with a ladder still adapting (under diminishing adaptation), with N_β the length of the interpolated values, we take the per-sweep trapezoid TI block as

$$\widehat{z}_t = \sum_{i=1}^{N_\beta} \Delta\beta_{i,t} \cdot S_{i,t}, \quad S_{i,t} = \frac{(\bar{\ell}_{i,t} + \bar{\ell}_{i+1,t})}{2} \quad (35)$$

With the S_t series, we estimate the multivariate long-run covariance Σ_S with multivariate OBM, and propagate with mean widths $\overline{d\beta} = \Delta\beta$:

$$\widehat{\sigma}_D^2 = \text{Var}[\widehat{z}_t] = \overline{d\beta}^\top \Sigma_S \overline{d\beta} \quad (36)$$

Note that for the total error, since $\widehat{\sigma}_D$ and $\widehat{\sigma}_S$ are added in quadrature, they are being treated as independent. For the adaptative case, we need a stationary adaptation settled in the ladder, which should happen under diminishing adaptations after some sweeps have passed, depending on the hyper-parameters on $\kappa(t)$ (see Eq.14).

References

- [1] Bruce Rannala and Ziheng Yang. Probability distribution of molecular evolutionary trees: A new method of phylogenetic inference. *Journal of Molecular Evolution*, 43:304–311, 09 1996.
- [2] Alexei Drummond, Geoff Nicholls, Allen Rodrigo, and Wiremu Solomon. Estimating mutation parameters, population history and genealogy simultaneously from temporally spaced sequence data. *Genetics*, 161:1307–20, 08 2002.
- [3] Ulrich H. E. Hansmann. Parallel tempering algorithm for conformational studies of biological molecules. *Chemical Physics Letters*, 281(1):140–150, December 1997.
- [4] Yuji Sugita and Yuko Okamoto. Replica-exchange molecular dynamics method for protein folding. *Chemical Physics Letters*, 314(1):141–151, November 1999.
- [5] Marc van der Sluys, Vivien Raymond, Ilya Mandel, Christian Röver, Nelson Christensen, Vicky Kalogera, Renate Meyer, and Alberto Vecchio. Parameter estimation of spinning binary inspirals using Markov chain Monte Carlo. *Classical and Quantum Gravity*, 25(18):184011, September 2008.
- [6] J. Veitch, V. Raymond, B. Farr, W. Farr, P. Graff, S. Vitale, B. Aylott, K. Blackburn, N. Christensen, M. Coughlin, W. Del Pozzo, F. Feroz, J. Gair, C. J. Haster, V. Kalogera, T. Littenberg, I. Mandel, R. O’Shaughnessy, M. Pitkin, C. Rodriguez, C. Röver, T. Sidery, R. Smith, M. Van Der Sluys, A. Vecchio, W. Vousden, and L. Wade. Parameter estimation for compact binaries with ground-based gravitational-wave observations using the LALInference software library. *prd*, 91(4):042003, February 2015.
- [7] James S. Jenkins, Matías R. Díaz, Nicolás T. Kurtovic, Néstor Espinoza, Jose I. Vines, Pablo A. Peña Rojas, Rafael Brahm, Pascal Torres, Pía Cortés-Zuleta, Maritza G. Soto, Eric D. Lopez, George W. King, Peter J. Wheatley, Joshua N. Winn, David R. Ciardi, George Ricker, Roland Vanderspek, David W. Latham, Sara Seager, Jon M. Jenkins, Charles A. Beichman, Allyson Bieryla, Christopher J. Burke, Jessie L. Christiansen, Christopher E. Henze, Todd C. Klaus, Sean McCauliff, Mayuko Mori, Norio Narita, Taku Nishiumi, Motohide Tamura, Jerome Pitogo de Leon, Samuel N. Quinn, Jesus Noel Villaseñor, Michael Vezie, Jack J. Lissauer, Karen A. Collins, Kevin I. Collins, Giovanni Isopi, Franco Mallia, Andrea Ercolino, Cristobal Petrovich, Andrés Jordán, Jack S. Acton, David J. Armstrong, Daniel Bayliss, François Bouchy, Claudia Belardi, Edward M. Bryant, Matthew R. Burleigh, Juan Cabrera, Sarah L. Casewell, Alexander Chaushev, Benjamin F. Cooke, Philipp Eigmüller, Anders Erikson, Emma Foxell, Boris T. Gänsicke, Samuel Gill, Edward Gillen, Maximilian N. Günther, Michael R. Goad, Matthew J. Hooton, James A. G. Jackman, Tom Louden, James McCormac, Maximiliano Moyano, Louise D. Nielsen, Don Pollacco, Didier Queloz, Heike Rauer, Liam Raynard, Alexis M. S. Smith, Rosanna H. Tilbrook, Ruth Titz-Weider, Oliver Turner, Stéphane Udry, Simon. R. Walker, Christopher A. Watson, Richard G. West, Enric Palle, Carl Ziegler, Nicholas Law, and Andrew W. Mann. An ultrahot Neptune in the Neptune desert. *Nature Astronomy*, 4:1148–1157, January 2020.
- [8] Jose I. Vines, James S. Jenkins, Zaira Berdiñas, Maritza G. Soto, Matías R. Díaz, Douglas R. Alves, Mikko Tuomi, Robert A. Wittenmyer, Jerome Pitogo de Leon, Pablo Peña, Jack J. Lissauer, Sarah Ballard, Timothy Bedding, Brendan P. Bowler, Jonathan Horner, Hugh R. A. Jones, Stephen R. Kane, John Kielkopf, Peter Plavchan, Avi Shporer, C. G. Tinney, Hui Zhang, Duncan J. Wright, Brett Addison, Matthew W. Mengel, Jack Okumura, and Anya Samadi-Ghadim. A dense mini-Neptune orbiting the bright young star HD 18599. *“MNRAS”*, 518(2):2627–2639, January 2023.
- [9] M. Mayor and D. Queloz. A Jupiter-Mass Companion to a Solar-Type Star. *Nature*, 378:355–+, November 1995.
- [10] Guillermo Gonzalez. The stellar metallicity-giant planet connection. *“MNRAS”*, 285(2):403–412, February 1997.
- [11] Geoffrey W. Marcy and R. Paul Butler. Planets Orbiting Other Suns. *PASP*, 112(768):137–140, February 2000.
- [12] E. B. Ford, V. Lystad, and F. A. Rasio. Planet-planet scattering in the upsilon Andromedae system. *Nature*, 434:873–876, April 2005.
- [13] P.C. Gregory. A Bayesian Analysis of Extrasolar Planet Data for HD 73526. *ApJ*, 631(2):1198–1214, October 2005.
- [14] Robert H. Swendsen and Jian-Sheng Wang. Replica Monte Carlo simulation of spin glasses. *prl*, 57(21):2607–2609, November 1986.
- [15] David J. Earl and Michael W. Deem. Parallel tempering: Theory, applications, and new perspectives. *Physical Chemistry Chemical Physics (Incorporating Faraday Transactions)*, 7(23):3910, January 2005.
- [16] J. Goodman and J. Weare. Ensemble samplers with affine invariance. *Comm. App. Math. Comp. Sci.*, 5:65, January 2010.

- [17] F. Hou, J. Goodman, D. W. Hogg, J. Weare, and C. Schwab. An Affine-invariant Sampler for Exoplanet Fitting and Discovery in Radial Velocity Data. *ApJ*, 745:198, February 2012.
- [18] John Skilling. Nested Sampling. In Rainer Fischer, Roland Preuss, and Udo Von Toussaint, editors, *Bayesian Inference and Maximum Entropy Methods in Science and Engineering*, volume 735 of *American Institute of Physics Conference Series*, pages 395–405, November 2004.
- [19] F. Feroz and M. P. Hobson. Multimodal nested sampling: an efficient and robust alternative to Markov Chain Monte Carlo methods for astronomical data analyses. *"MNRAS"*, 384(2):449–463, February 2008.
- [20] F. Feroz, S. T. Balan, and M. P. Hobson. Detecting extrasolar planets from stellar radial velocities using Bayesian evidence. *"MNRAS"*, 415(4):3462–3472, August 2011.
- [21] Edward Higson, Will Handley, Mike Hobson, and Anthony Lasenby. Dynamic nested sampling: an improved algorithm for parameter estimation and evidence calculation. *Statistics and Computing*, 29(5):891–913, September 2019.
- [22] Joshua S. Speagle. DYNESTY: a dynamic nested sampling package for estimating Bayesian posteriors and evidences. *"MNRAS"*, 493(3):3132–3158, April 2020.
- [23] Hannah Diamond-Lowe, David Charbonneau, Matej Malik, Eliza M. R. Kempton, and Yuri Beletsky. Optical Transmission Spectroscopy of the Terrestrial Exoplanet LHS 3844b from 13 Ground-based Transit Observations. *AJ*, 160(4):188, October 2020.
- [24] Wangang Xie, Paul Lewis, Yu Fan, Lynn Kuo, and Ming-Hui Chen. Improving marginal likelihood estimation for bayesian phylogenetic model selection. *Systematic biology*, 60:150–60, 03 2011.
- [25] Andrew Gelman and Xiao-Li Meng. Simulating normalizing constants: From importance sampling to bridge sampling to path sampling. *Statistical Science*, 13:163–185, 1998.
- [26] Andrew Gelman, John B. Carlin, Hal S. Stern, and Donald B. Rubin. *Bayesian Data Analysis*. Chapman and Hall/CRC, 2nd ed. edition, 2004.
- [27] Jamie R. Oaks, Kerry A. Cobb, Vladimir N. Minin, and Adam D. Leaché. Marginal likelihoods in phylogenetics: a review of methods and applications. *arXiv e-prints*, page arXiv:1805.04072, May 2018.
- [28] Patricio Maturana-Russel, Renate Meyer, John Veitch, and Nelson Christensen. Stepping-stone sampling algorithm for calculating the evidence of gravitational wave models. *prd*, 99(8):084006, April 2019.
- [29] Blazej Miasojedow, Eric Moulines, and Matti Vihola. Adaptive parallel tempering algorithm. *arXiv e-prints*, page arXiv:1205.1076, May 2012.
- [30] Paul M. Goggans and Ying Chi. Using Thermodynamic Integration to Calculate the Posterior Probability in Bayesian Model Selection Problems. In Gary J. Erickson and Yuxiang Zhai, editors, *Bayesian Inference and Maximum Entropy Methods in Science and Engineering*, volume 707 of *American Institute of Physics Conference Series*, pages 59–66, April 2004.
- [31] Nicolas Lartillot and Hervé Philippe. Computing bayes factors using thermodynamic integration. *Systematic biology*, 55:195–207, 05 2006.
- [32] Cristian Predescu, Mihaela Predescu, and Cristian V. Ciobanu. The incomplete beta function law for parallel tempering sampling of classical canonical systems. *J. Chem. Phys.*, 120(9):4119–4128, March 2004.
- [33] Aminata Kone and David Kofke. Selection of temperature intervals for parallel-tempering simulations. *The Journal of chemical physics*, 122:206101, 06 2005.
- [34] Gareth Roberts and Jeffrey Rosenthal. Coupling and ergodicity of adaptive markov chain monte carlo algorithms. *Journal of Applied Probability - J APPL PROBAB*, 44, 03 2007.
- [35] W. D. Vosuden, W. M. Farr, and I. Mandel. Dynamic temperature selection for parallel tempering in Markov chain Monte Carlo simulations. *"MNRAS"*, 455(2):1919–1937, January 2016.
- [36] David Kofke. On the acceptance probability of replica-exchange monte carlo trials. *jcpb*, 117:6911–, 10 2002.
- [37] Walter R. Gilks, Gareth O. Roberts, and Sujit K. Sahu. Adaptive markov chain monte carlo through regeneration. *Journal of the American Statistical Association*, 93(443):1045–1054, 1998.
- [38] Nitin Rathore, Manan Chopra, and Juan de Pablo. Optimal allocation of replicas in parallel tempering simulations. *The Journal of chemical physics*, 122:024111, 02 2005.
- [39] Helmut G. Katzgraber, Simon Trebst, David A. Huse, and Matthias Troyer. Feedback-optimized parallel tempering Monte Carlo. *Journal of Statistical Mechanics: Theory and Experiment*, 2006(3):03018, March 2006.

- [40] Daniel K. Shenfeld, Huafeng Xu, Michael P. Eastwood, Ron O. Dror, and David E. Shaw. Minimizing thermodynamic length to select intermediate states for free-energy calculations and replica-exchange simulations. *Phys. Rev. E*, 80:046705, Oct 2009.
- [41] James M. Flegal and Galin L. Jones. Batch means and spectral variance estimators in Markov chain Monte Carlo. *arXiv e-prints*, page arXiv:0811.1729, November 2008.
- [42] Yu-Bo Wang, Ming-Hui Chen, Lynn Kuo, and Paul O. Lewis. A New Monte Carlo Method for Estimating Marginal Likelihoods. *Bayesian Analysis*, 13(2):311 – 333, 2018.
- [43] F. N. Fritsch and J. Butland. A method for constructing local monotone piecewise cubic interpolants. *SIAM Journal on Scientific and Statistical Computing*, 5(2):300–304, 1984.
- [44] X.-L. Meng and W.H. Wong. Simulating ratios of normalizing constants via simple identity: a theoretical exploration. *Statistica Sinica*, 6:831–860, 1996.
- [45] Quentin F. Gronau, Alexandra Sarafoglou, Dora Matzke, Alexander Ly, Udo Boehm, Maarten Marsman, David S. Leslie, Jonathan J. Forster, Eric-Jan Wagenmakers, and Helen Steingroever. A Tutorial on Bridge Sampling. *arXiv e-prints*, page arXiv:1703.05984, March 2017.
- [46] Filippo Pagani, Martin Wiegand, and Saralees Nadarajah. An n-dimensional Rosenbrock Distribution for MCMC Testing. *arXiv e-prints*, page arXiv:1903.09556, March 2019.
- [47] F. Pepe, C. Lovis, D. Ségransan, W. Benz, F. Bouchy, X. Dumusque, M. Mayor, D. Queloz, N. C. Santos, and S. Udry. The HARPS search for Earth-like planets in the habitable zone. I. Very low-mass planets around <ASTROBJ>HD 20794</ASTROBJ>, <ASTROBJ>HD 85512</ASTROBJ>, and <ASTROBJ>HD 192310</ASTROBJ>. *A&A*, 534:A58, October 2011.
- [48] N. Nari, X. Dumusque, N. C. Hara, A. Suárez Mascareño, M. Cretignier, J. I. González Hernández, A. K. Stefanov, V. M. Passegger, R. Rebolo, F. Pepe, N. C. Santos, S. Cristiani, J. P. Faria, P. Figueira, A. Sozzetti, M. R. Zapatero Osorio, V. Adibekyan, Y. Alibert, C. Allende Prieto, F. Bouchy, S. Benatti, A. Castro-González, V. D'Odorico, M. Damasso, J. B. Delisle, P. Di Marcantonio, D. Ehrenreich, R. Génova-Santos, M. J. Hobson, B. Lavie, J. Lillo-Box, G. Lo Curto, C. Lovis, C. J. A. P. Martins, A. Mehner, G. Micela, P. Molaro, C. Mordasini, N. Nunes, E. Palle, S. P. Quanz, D. Ségransan, A. M. Silva, S. G. Sousa, S. Udry, N. Unger, and J. Venturini. Revisiting the multi-planetary system of the nearby star HD 20794: Confirmation of a low-mass planet in the habitable zone of a nearby G-dwarf. *A&A*, 693:A297, January 2025.
- [49] Daniel Foreman-Mackey, David W. Hogg, Dustin Lang, and Jonathan Goodman. emcee: The MCMC Hammer. *PASP*, 125(925):306, March 2013.
- [50] Digital Science UK Ltd. Overleaf, 2025.